Ultra-small polydopamine nanomedicine-enabled antioxidation against senescence

Jiamei Han [a], Jiao Wang [a], Hongwei Shi [a], Qian Li [b,c], Shibo Zhang [a], Hao Wu [a], Wenjun Li [a], Linhua Gan [d], Holly M. Brown-Borg [e,****], Wei Feng [a,***], Yu Chen [a,**], Robert Chunhua Zhao [a,b,*]

[a] School of Life Sciences, Shanghai University, Shanghai, China
[b] Institute of Basic Medical Sciences Chinese Academy of Medical Sciences, School of Basic Medicine Peking Union Medical College, Center of Excellence in Tissue Engineering, Chinese Academy of Medical Sciences, Beijing Key Laboratory of New Drug Development and Clinical Trial of Stem Cell Therapy (BZ0381), Beijing, China
[c] Cell Energy Life Sciences Group Co. LTD, Qingdao, Shandong, China
[d] Department of Neurology and National Research Center for Aging and Medicine & National Center for Neurological Disorders, State Key Laboratory of Medical Neurobiology, Huashan Hospital, Fudan University, Shanghai, China
[e] Department of Biomedical Sciences, School of Medicine & Health Sciences, University of North Dakota, Grand Forks, ND, USA

ARTICLE INFO

ABSTRACT

Senescence is a cellular response characterized by cells irreversibly stopping dividing and entering a state of permanent growth arrest. One of the underlying pathophysiological causes of senescence is the oxidative stress-induced damage, indicating that eliminating the reactive oxygen and nitrogen species (RONS) may be beneficial to prevent and/or alleviate senescence. Herein, we developed ultra-small polydopamine nanoparticles (UPDA NPs) with superoxide dismutase (SOD)/catalase (CAT) enzyme-mimic activities, featuring broad-spectrum RONS-scavenging capability for inducing cytoprotective effects against RONS-mediated damage. The engineered UPDA NPs can restore senescence-related renal function, tissue homeostasis, fur density, and motor ability in mice, potentially associated with the regulation of multiple genes involved in lipid metabolism, mitochondrial function, energy homeostasis, telomerase activity, neuroprotection, and inflammatory responses. Importantly, the dietary UPDA NPs can enhance the antioxidant capacity, improve the climbing ability, and prolong the lifespan of *Drosophila*. Notably, UPDA NPs possess excellent biocompatibility stemming from the ultra-small size, ensuring quick clearance out of the body. These findings reveal that UPDA NPs can delay aging through reducing oxidative stress and provide a paradigm and practical strategy for treating senescence and senescence-related diseases.

1. Introduction

Senescence or biological aging is a state of irreversible cell growth arrest accompanied with the halt of cell division before cells reach the end of their lifespan [1]. Senescence can lead to systemic changes, which are associated with various chronic diseases such as Alzheimer's disease [2], diabetes [3], atherosclerosis [4] and cancer [5], posing a heavy burden on society, both medically and economically. In addition to natural aging, senescence occurs in response to various noxious stimuli, including DNA damage, oncogenic stress, telomere dysfunction, inflammation, mitochondrial dysfunction, epigenetic alterations, proteostasis

imbalance, dysregulated intracellular signaling pathways, and oxidative stress [6,7]. The free radical theory of aging posits that aging-associated functional losses result from the accumulation of oxidative damage caused by reactive oxygen and nitrogen species (RONS), referring to reactive radical and non-radical derivatives of oxygen and nitrogen, such as superoxide anion radical ($O_2^{\bullet-}$) [8], hydrogen peroxide (H_2O_2), hydroxyl radical ($\bullet OH$) [9], nitric oxide radical ($\bullet NO$), and peroxynitrite anion ($ONOO^-$), continuously produced in the process of cell metabolism or upon the stimulation of environmental factors [10]. As one of the fundamental mechanisms driving aging, oxidative stress has received continued and even increasing attention, which is a phenomenon

---

characterized by the imbalance between RONS-related oxidants and antioxidants [11]. RONS, whether endogenous or exogenous, induce the oxidative modification of most biological macromolecules involving proteins, lipids, carbohydrates, and nucleic acids, and further change their stability and function [11]. Therefore, there is an urgent need to develop effective strategies to eliminate or reduce excessive RONS for delaying the aging process.

Living organisms possess a series of highly effective enzymes including catalase (CAT) [12] and superoxide dismutase (SOD) [13] with the ability to remove RONS, protecting tissues or organs from oxidative damage. These natural antioxidant enzymes are a class of biomolecules (*e.g.,* proteins and RNA), which are typically sensitive to non-physiological or adverse environmental conditions (*e.g.*, extreme temperature and pH) [14,15] making them difficult to produce in large quantities. Also, the activity of these enzymes relies on the binding of mineral elements, such as copper, iron, manganese, and zinc, the intake of which can be greatly compromised because of aging or aging-related diseases [16]. To address such challenges, a number of artificial enzymes mimicking the activities of natural enzymes have been developed [17,18], including nanozymes which have combined advantages, such as ease of production, low cost, multifunction and high stability. Among them, common inorganic nanozymes such as CeO_2 [19], platinum [20], V_2O_5 [21] and 2D carbides and nitrides (MXenes) [22] with RONS-scavenging ability have been potentially applied in various diseases including hepatic ischemia-reperfusion injury [23], neurodegenerative diseases (*e.g.*, Alzheimer's [24] and Parkinson's [25] diseases), acute kidney injury [26] and so on. However, questions have been raised regarding the biosafety and biocompatibility of inorganic materials, as some have been reported to interact with biomolecules including DNAs, proteins and lipids [27]. To date, non-negligible toxicity issues in biological systems (cells, tissues, organs, *etc.*) have restricted inorganic nanozymes for further clinical translation [28].

Compared to inorganic nanozymes, organic nanozymes exhibit satisfactory biocompatibility and chemical flexibility [29]. During the last decade, an increasing number of organic nanozymes have been developed for the detection of biomolecues or the treatment of cancer [30], while rarely proposed for combating oxidative stress-related diseases. This is partly due to the fact that organic nanozymes are generally designed to mimic the catalytic activity of specific enzymes, which renders them insufficient to clear multiple types of RONS that can be overproduced concomitantly in the progression of aging or aging-related diseases. Therefore, developing nanoparticles with multiple-enzyme properties is essential to overcome this limitation.

Polydopamine (PDA), which is widely used for synthesizing artificial melanin particles, has significant advantages in terms of biosafety [31]. In previous reports, PDA is widely utilized as a theranostic agent in the biomedical field ascribing to its binding affinity to metal ions and response to various external stimuli such as light, pH, and ultrasonic/magnetic field. A recent study showed that PDA is redox-active and can either accept electrons from reducing agents or donate electrons to oxidants with an effect of quenching free radicals [32]. Based on these two distinct properties, both the antimicrobial activities and scavenging potentials for reactive oxygen species (ROS) of PDA have been reported [30,32–34]. As PDA is enriched with the reductive groups of catechol similar to natural polymer melanin and the size of melanin-like nanoparticles can be easily adjusted with the alkali-based self-polymerization technique, the antioxidative enzyme-like activities of PDA with ROS scavenging performances are worthwhile to investigate for further *in vivo* application. Particularly, downscaling the size of polymers may not only make them bioexcretable but also expand their contact area with the free radicals, which can maximize their anti-aging effects by enhancing the electron-donating capacity. Herein, we designed and developed ultra-small polydopamine nanoparticles (UPDA NPs) *via* liquid-phase exfoliation technology, which are integrated with CAT/SOD mimetic cascade activities and broad-spectrum ROS-scavenging capabilities, capable of catalyzing $O_2^{\bullet-}$ to generate H_2O_2 and O_2, decomposing H_2O_2

into H_2O and O_2, and removing •OH. Additionally, UPDA NPs can serve as a scavenger for reactive nitrogen species (RNS) such as •NO and $ONOO^-$. We verified that UPDA NPs inhibit oxidative stress-induced senescence *in vitro*. Further evaluation demonstrated that UPDA NPs possess excellent biocompatibility and biosafety, and display anti-aging effects *in vivo*. Transcriptomics analysis revealed that the anti-senescence effects of UPDA NPs are likely related to but not limited to the regulation of the NF-κB signaling pathway. Particularly, UPDA NPs can rescue drug-induced senescent behaviors in mice and can effectively restore the lifespan of *Drosophila* under oxidative stress (Fig. 1). These results not only demonstrate that UPDA NPs can be used as a paradigm of anti-aging nanomedicine that exhibits desirable RONS-scavenging performance with potential clinical application prospect, but also provide an alternative and efficient strategy for the alleviation and treatment of senescence.

2. Material and methods

2.1. Experimental design

This study was designed to develop an ultra-small organic nanomedicine (UPDA NPs) with good biocompatibility and anti-senescence effects. For the synthesis of UPDA NPs, we used techniques of self-polymerization and liquid-phase exfoliation. A wide range of imaging and spectroscopic analysis were performed for the characterization of UPDA NPs. For evaluating the antioxidation effects of UPDA NPs, we determined their RONS-scavenging efficacies and SOD/CAT activities. For confirming the biocompatibility and biosafety of UPDA NPs *in vivo*, we examined the major organs and hematological parameters of mice. To assess the suppressive effects of UPDA NPs on oxidative stress-induced senescence, different senescent models (doxorubicin (DOX)-treated human 293 T cells, DOX-treated mice, and D-galactose (D-gal)-treated *Drosophila*) were used for determining the expression levels of senescence-associated secretory phenotype (SASP)-related molecules. For understanding the anti-senescence mechanism of UPDA NPs, transcriptomics analysis was performed to identify differentially expressed genes (DEGs) and relevant pathways in the kidneys of DOX-treated mice. To explore the possibility of applying UPDA NPs in the treatment of senescence, we carried out phenotype evaluation, physiological function assessment and behavioral studies in DOX-treated mice and D-gal-treated *Drosophila*.

2.2. Chemical materials

Dopamine hydrochloride, sodium hydroxide (NaOH), sodium nitrite ($NaNO_2$), doxorubicin hydrochloride, 1,1-Diphenyl-2-picrylhydrazyl radical (DPPH·), DETA NONOate (NOC18), 5,5-dimethyl-1-pyrrolineN-oxide (DMPO), 4,5-Dihydro-4,4,5,5-tetramethyl-2-phenyl-1H-imidazol-1-yloxy-1-oxide (PTIO), X-Gal (5-bromo-4-chloro-3-indolyl-β-D-galactoside), and dihydroethidium (DHE) were purchased from Meryer (Shanghai) Chemical Technology. Phosphate-buffered saline (PBS, pH 7.4, Na_2HPO_4–NaH_2PO_4, 10 mM) solution was prepared in the laboratory. All chemicals and reagents were of analytical grade and used as received without further purification. Ultrapure water (18.2 MΩ cm^{-1} at 25 °C) purified by a Milli-Q system was used throughout the experiment.

2.3. Transmission electron microscope (TEM) imaging and spectroscopic analyses

TEM imaging was conducted on a JEM-1400Flash electron microscope (JEOL, Japan) at 120 kV. The sample was prepared by dispersing a small amount of freeze-dried powder in PBS. Then, the suspension was dropped on 230 mesh copper TEM grids covered with thin amorphous carbon films. Fourier transform infrared spectrum (FT-IR) spectra were measured by a VERTEX70 spectrometer (Bruker, Germany) in the range of 4000–400 cm^{-1}. Ultraviolet visible (UV–vis) spectra were obtained
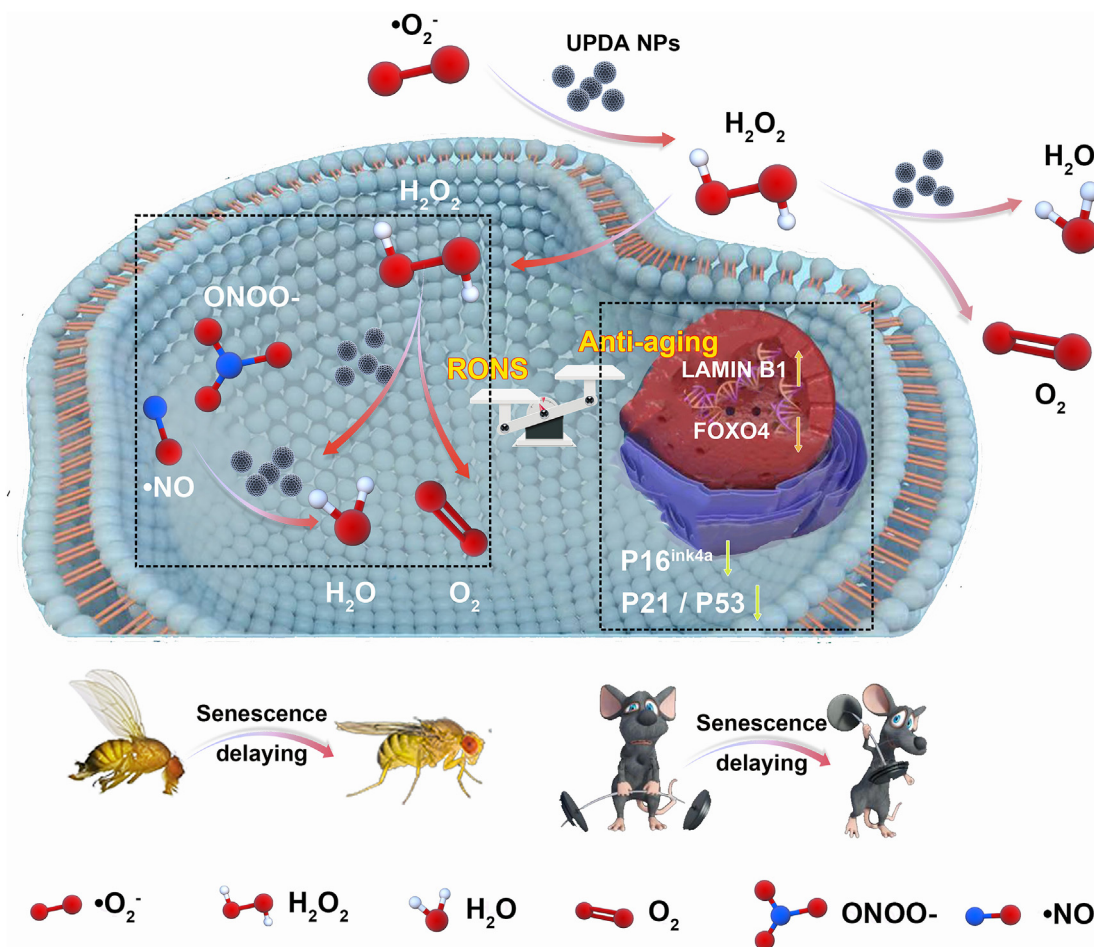
Fig. 1. Schematic illustration of the underlying process and mechanism of UPDA NPs in the efficient treatment for cellular senescence and aging of model organisms. UPDA NPs can turn toxic ROS into non-toxic substances. Specifically, $O_2^{\bullet-}$ is converted to H_2O_2 and O_2, and H_2O_2 is decomposed to O_2 and H_2O, mimicking the activities of SOD and CAT. Harmful RNS including •NO and ONOO$^-$ can also be removed by UPDA NPs. The RONS-scavenging capacities of UPDA NPs are translated to the reversion of senescent phenotypes and behaviors in *Drosophila* and mice, represented by the regulation of key senescence mediators at the cellular and molecular levels.

using a VNANODROP 8000 spectrometer (Thermofisher scientific, U.S.A). A dynamic light scattering (DLS) particle size analyzer (Malvern 2000, U.S.A) was used to determine the hydrophilic diameters of the particles. X-ray photoelectron spectroscopy (XPS) was performed with an ESCALAB 250Xi (Thermofisher scientific, U.S.A) X-ray source. The crystal structure and oxidation state of UPDA NPs were analyzed using a X-ray diffractometer (Smartlab, China). The electron spin resonance (ESR) spectroscopy signal was obtained on a Bruker A300 (X-band) spectrometer (Bruker, Germany). All the measurements were performed at room temperature if not specified otherwise.

2.4. Preparation of UPDA NPs

180 mg of dopamine hydrochloride was dissolved in 90 mL of deionized water. 840 µL of 1 mol L^{-1} (M) NaOH solution was added to the dopamine hydrochloride solution at 60 °C and the mixture underwent vigorous stir. The reaction lasted for 5 h. The solution color turned to pale yellow as soon as NaOH was added and gradually changed to dark brown. The product was collected by centrifugation at 16,000 rpm for 20 min and was then washed with deionized water three times. The aqueous solvent was removed by freeze-drying to obtain black solids of PDA. Under vigorous stir, 20 mg PDA nanoparticles was dissolved in 10 mL of 0.1 M NaOH. Then we swiftly dropped 0.1 M HCl into the obtained solution to adjust the pH to 7.0 under sonication with an output power of 600 W for 2 min. We obtained a bright black PDA solution. The particles

were retrieved by centrifugation with a centrifugal filter (centrifugal filter device, MWCO = 30 kDa) at 8000 rpm for 8 min and was washed several times with deionized water to remove the byproduct NaCl, followed by freeze-drying to obtain black solids of UPDA NPs.

2.5. Determination of RONS-scavenging capability

The evaluation of 2,2′-azino-bis(3-ethylbenzothiazoline-6-sulphonic acid) (ABTS) radical scavenging activity was performed according to a previously reported method [22]. Briefly, the ABTS radicals (ABTS•$^+$) were generated by incubating 7 mM ABTS stock solution with 2.45 mM potassium persulfate in dark for 16 h. Then, the ABTS•$^+$ solution was diluted with PBS to reach an absorbance at 405 nm. 2 mL UPDA NPs solutions (0, 20, 40, and 60 µg mL^{-1}, respectively) were mixed with 2 mL ABTS solution and were placed in dark for 10 min. Then the absorbance at 405 nm was monitored with a UV–vis spectrophotometer. The ABTS•$^+$ scavenging abilities were calculated as follows:

$$\text{ABTS}\bullet^+ \text{ scavenging ratio } (\%) = \left(\left(A_{control} - A_{sample} \right) / A_{control} \right) \times 100,$$

where $A_{control}$ is the absorbance of a standard solution without any radical scavengers, and A_{sample} is the absorbance after the reaction with the radical scavengers, respectively.

The SOD-like activity was determined using an WST-1 (2-(4-iodophenyl)-3-(4-nitrophenyl)-5-(2,4-disulfophenyl)-2H-tetrazolium) assay

kit (Nanjing Jiancheng Bioengineering Institute, China) according to the manufacturer's instruction. Briefly, a tetrazolium salt WST-1 reacts with O_2^-, generating a formazan dye with a characteristic absorption at 450 nm. This reaction is inhibited by SOD due to the disproportionation of O_2^-. Therefore, the SOD-like activity is negatively correlated with the absorbance value of the formazan dye, which was measured with the addition of different concentrations of UPDA NPs (20, 40, 60, 90, 160, 190, 30, and 340 µg mL^{-1}) using a multiple plate reader (Molecular Devices, U.S.A).

The CAT-like activity was determined based on the H_2O_2 decomposition reaction. A tube containing 10 mM H_2O_2 and 0.1 mM 3-carbamoyl-2,2,5,5-tetramethyl-3-pyrrolin-1-yloxy (CTPO) in PBS was pumped with N_2 for 10 min. Then, UPDA NPs (1.25, 12.5, and 50 µg mL^{-1}) was added and incubated for 5 min. ESR spectra were monitored at different time points. In the steady-state kinetic assay for determining the CAT-like catalytic mechanism, a detection kit for H_2O_2 (Beyotime, China) was used. Briefly, H_2O_2 of different concentrations (5–60 µM) was added to 100 µg mL^{-1} UPDA NPs in separate test tubes. The detection solution was added and the reaction mixture was incubated at room temperature for 30 min. Then, the absorbance values were measured at 640 nm and the dynamics curve was registered on a UV–vis spectrophotometer. The Michaelis-Menten constant (K_m) of UPDA NPs-catalyzed reaction was obtained by plotting the initial velocity versus H_2O_2 concentration. The maximum velocity (V_{max}) was calculated from the Lineweaver-Burk plot, where $1/V = 1/V_{max} + K_m (V_{max}C)$.

The amount of •OH was measured with the Fenton reaction, in which •OH causes methylene blue (MB) to oxidize and its color fading degree is proportional to the amount of •OH. Different concentrations of UPDA NPs (0, 45, and 90 µg mL^{-1}) were added to the •OH-MB reaction solution, and the absorbance at 664 nm was measured. The •OH-scavenging rate was obtained with the following equation:

$$Inhibition\ (\%) = \left(\left(A_{sample} - A_{control} \right) / A_{sample} \right) \times 100,$$

where $A_{control}$ is the absorbance of the control group, and A_{sample} is the absorbance of the UPDA NPs-treated group.

DPPH• was used to evaluate the RNS scavenging activity of UPDA NPs. Different concentrations of UPDA NPs (0, 5, 25, and 100 µg mL^{-1}) were mixed with 40 µM DPPH• for 12 h and the absorbance spectra at 532 nm were recorded.

The ·NO-scavenging ability of UPDA NPs (50 µg mL^{-1}) was tested by ESR spectroscopy using carboxy-PTIO (2-(4-Carboxyphenyl)-4,4,5,5-tetramethylimidazoline-1-oxyl-3-oxide) as the trapper and the detection dye for ·NO. NOC18 was used as the source of ·NO. Carboxy-PTIO was dissolved in phosphate buffer (250 mM, pH 7.4), and NOC18 was dissolved in NaOH (1 mM). In a test tube, 0.5% methylcellulose was mixed with NOC18 (5 µM) for 30 min at room temperature, and the mixture was then added into the carboxy-PTIO solution (5 µM) in the absence or presence of UPDA NPs. The ESR spectra were then recorded. The ESR signal of carboxy-PTIO is characterized by five peaks. ·NO from NOC18 can reduce carboxy-PTIO to carboxy-PTI and generate ·NO$_2$, which shows seven peaks of ESR signals. The reduction of carboxy-PTIO by ·NO leads to a color change from purple to yellow.

The ONOO$^-$-scavenging ability of UPDA NPs (0, 25, and 100 µg mL^{-1}) was evaluated by UV–vis spectroscopy using pyrogallol red as the indicator. The absorbance values were measured at 545 nm.

2.6. Cell culture

The 293 T cell line was acquired from ATCC, and cultured in dulbecco's modified eagle medium (DMEM) (Hyclone, U.S.A) containing 10% Foetal Bovine Serum (FBS) (Gibco, U.S.A) and 1% s7 penicillin/streptomycin (Gibco, U.S.A) at 37 °C with 5% CO_2. For DOX-induced senescence, 293 T cells were treated twice with 0.2 mM DOX with a 2-day interval and were analyzed 7 days later. The expression of

β-galactosidase was detected by the cleavage of X-Gal. The levels of IL-6 and IL-1β were determined using commercially available kits (Boster Bio, China) and quantified from 3 replicates (n = 3).

2.7. Measurement of ROS scavenging activities in vitro

293 T cells were seeded into 96-well and 24-well plates at a density of 1×10^4 cells per well and 1×10^5 cells per well, respectively. After incubation for 24 h, cells were treated with 2×10^{-7} M DOX, 8 g/L D-gal, or 250 µM H_2O_2 and 100 µg mL^{-1} UPDA NPs, were further incubated at 37 °C for a 2-day interval, and were analyzed 7 days later. For determining cell viability, cells seeded in 96-well plates were evaluated with cell counting kit-8 (CCK-8, Beyotime, China). Cells without the addition of UPDA NPs were regarded as the control. At least 50,000 cells were analyzed in each sample. For determining the ROS-scavenging effect of UPDA NPs (20 µg mL^{-1}), dichlorofluorescein (DCF), an oxidation sensitive fluorescent dye, was used to detect the intracellular ROS level [35]. Briefly, DCFH-DA (2′,7′-dichlorodihydrofluorescein diacetate) is a non-fluorescent chemical compound which can diffuse through the cell membrane freely and can be hydrolyzed by an intracellular esterase to generate DCFH (2′,7′-dichlorodihydrofluorescein). The non-fluorescent DCFH can be oxidized by the intracellular ROS to form fluorescent DCF. Therefore, the quantity of intracellular ROS is correlated with the fluorescent intensity of DCF. After the aforementioned incubation, cells were gently rinsed three times with serum-free medium to remove the free UPDA NPs. Then, 10 µM DCFH-DA in serum-free medium was added to the cells, followed by incubation in dark at 37 °C for 30 min. Afterwards, the cells were washed with serum-free medium three times to remove unloaded DCFH-DA probe, imaged using a laser confocal microscope (Zeiss, Germany), and subjected to flow cytometric analysis.

2.8. Immunocytochemistry

Normal and DOX-induced senescent 293 T cells were fixed with 4% paraformaldehyde (PFA) for 15 min, permeabilized with 0.2% Triton X-100 for 3 min and was then blocked with 10% (v/v) BSA (bovine serum albumin) in PBS for 2 h at room temperature or at 4 °C overnight. Subsequently, the cells were washed with PBS three times and were then incubated with primary antibodies rabbit anti-Forkhead box O4 protein (FOXO4) (1:150, Proteintech, U.S.A), rabbit anti-p16^{ink4a} (1:150, Abclonal, China), or rabbit anti-lamin B1 (1:150, Abclonal, China) for 2 h. After the incubation, the cells were washed three times with PBS and incubated with goat anti-rabbit IgG H&L Alexa Fluor® 488 (1:200, Abcam, UK) for 2 h. Then, after three washes with PBS, the cells were stained with DAPI for 5 min, followed by another three washes with PBS. Finally, the cells were mounted and imaged on an inverted fluorescence microscope (Zeiss, Germany). The fluorescence intensity was obtained from 3 randomly selected regions of the cell culture to determine the expression levels of FOXO4, p16^{ink4a}, and lamin B1 in each group. Three independent batches of cells were analyzed to determine the significance of difference between different groups.

2.9. Western blotting

293 T cells (1.0×10^6) were collected and total protein was extracted with RIPA (Radioimmunoprecipitation) lysis buffer (Beyotime, China). The protein lysates were then separated by SDS-PAGE and transferred to nitrocellulose filter membranes. The membranes were incubated with primary antibodies rabbit anti-p21 (1:1000, ABclonal, China), rabbit anti-lamin B1(1:1000, Abcam, UK), rabbit anti-decoy receptor 2 (DcR2) (1:1000, Proteintech, U.S.A), or mouse anti-glyceraldehyde 3-phosphate dehydrogenase (GAPDH) (1:10,000, ABclonal, China) and then with goat anti-rabbit IgG (H + L) DyLight™ 800-Labeled or goat anti-mouse IgG (H + L) DyLight™ 680-Labeled secondary antibodies (1:10,000, KPL,

U.S.A). The immune-positive bands were visualized using an Odyssey scanner (LI-COR Biosciences, USA). The band densities of p21, lamin B1, and DcR2 were quantified in ImageJ and normalized against those of GAPDH, representing their protein expression levels respectively.

2.10. Animals

The animal care and experimental procedures were approved by the Animal Ethics Committee of Shanghai University (ECSHU 2021–039). A maximum of four mice per cage were kept on a 12-h light/dark cycle at a constant temperature (22 °C) with food and water *ad libitum*. C57BL/6J mice of 26 weeks were used for DOX-induced senescent model. Mice were given two intraperitoneal injections of DOX at a dose of 10 mg/kg. All mice were kept in group housing until the start of the experiment and were then randomly assigned to control and experimental groups.

2.11. Biocompatibility and biosafety evaluation

C57BL/6J mice (2 months old, 20–25 g) were intravenously administrated with UPDA NPs at a single dose of 200 μL (100 μg mL^{-1}). The mice injected with PBS were used as the control group. At day 30 post injection, the mice were anesthetized with intraperitoneal injection of chloral hydrate and sacrificed to harvest major organs (including heart, liver, spleen, lung, and kidney) for hematoxylin and eosin staining and histological analysis. Mouse blood was collected through cardiac puncture. Routine blood parameters, including white blood cells (WBC), lymphocytes (LYM), monocytes (MON), granulocytes (GRA), mean platelet volume (MPV), red blood cells (RBC), hemoglobin (HGB), mean corpuscular hemoglobin (MCH), hematocrit (HCT), red blood cell distribution width-standard deviation (RDWSD), mean corpuscular volume (MCV), mean corpuscular-hemoglobin concentration (MCHC), platelet (PLT), platelet distribution width (PDW), and red blood cell distribution width-coefficient of variation (RDWCV), were analyzed on a Sysmex XS-800i automated hematology analyzer (Sysmex, Japan).

2.12. Immunohistochemistry

Mice were anesthetized and perfused with PBS. The kidneys were collected, fixed with 4% PFA, and cut to obtain 30 μm sections using a vibratome (Invitrogen, U.S.A). After three rinses in PBS (5 min each), the sections were blocked in PBST (PBS + 0.3% Triton X-100) with 3% BSA for 2 h, and were then incubated in primary antibodies rabbit anti-lamin B1 (Abclonal, China), mouse anti-p53 (Abcam, UK) or rabbit anti-p21 (ABclonal, China) with a dilution of 1:1000 at 4 °C for 24 h, followed by three rinses in PBS. Then, the sections were incubated with goat anti-rabbit IgG H&L Alexa Fluor® 488 (1:300, Abcam, UK) or goat anti-mouse IgG H&L Alexa Fluor® 488 secondary antibodies (1:300, Abcam, UK) for 2 h at room temperature. After the incubation, the sections were washed with PBS for 5 min, and the nuclei were counterstained with DAPI for 5 min. Finally, the sections were washed in PBST and mounted in mounting medium. Fluorescence images were acquired with a 20 × objective on a confocal microscope.

Flies were anesthetized with CO_2, dissected in PBS, and fixed with 4% PFA at room temperature. Brain sections were prepared and incubated with rabbit anti-caspase-3 primary antibody (1:500, Beyotime, China) and then with goat anti-rabbit IgG H&L Alexa Fluor® 488 (1:200, Abcam, UK), followed by DAPI staining and fluorescence imaging.

2.13. Determination of renal and hepatic function parameters

Blood samples were acquired from normal mice and DOX-induced senescent mice with or without the treatment of UPDA NPs for plasma separation. These samples were then centrifuged for 10 min at 1200 g. The supernatants were transferred into 1.5 mL tubes and recentrifuged for 5 min at 1200 g. The supernatants were transferred again into 1.5 mL tubes for determining the levels of creatinine (CRE), blood urea nitrogen

(BUN), alanine transaminase (ALT), and aspartate aminotransferase (AST).

2.14. Assessment of swimming performance

We monitored the swimming behavior of different mouse groups by continuously measuring their swimming speed. Swimming activity was recorded for 30 days.

2.15. Transcriptomics analysis

DOX-induced senescent mice were randomly divided into two groups: the control group (n = 5) and the group treated with 100 μg mL^{-1} UPDA NPs at a dosage of 200 μL (experimental group, n = 5). After 24 h post injection, mice were sacrificed to collect the kidneys. Total RNA was extracted using TRIzol® Reagent (Invitrogen, U.S.A) according to the manufacturer's instructions and genomic DNA was removed using DNase I (Takara Bio, U.S.A). Then RNA quality was determined by a 2100 Bioanalyser (Agilent, U.S.A) and quantified using an ND-2000 instrument (NanoDrop Technologies, U.S.A). Only high-quality RNA samples (OD260/280 = 1.8–2.2, OD260/230 ≥ 2.0, RIN≥6.5, 28S:18S ≥ 1.0, >1 μg) were used to construct sequencing library. RNA-seq transcriptome library was prepared with a TruSeqTM RNA sample preparation Kit (Illumina, U.S.A) using 1 μg of total RNA. Briefly, messenger RNA with polyA tails was captured by oligo (dT) beads and was then fragmented in fragmentation buffer. Next, double-stranded cDNA was synthesized using a SuperScript double-stranded cDNA synthesis kit (Invitrogen, U.S.A) with random hexamer primers (Illumina, U.S.A). The synthesized cDNA was subjected to end-repair, phosphorylation, and adenylation on the 3′ end. Libraries were enriched for cDNA fragments of 300 bp on 2% Low Range Ultra Agarose gels followed by PCR amplification using Phusion DNA polymerase (NEB, U.S.A) for 15 PCR cycles. After the quantification with a TBS380 fluorometer (Turner BioSystems, U.S.A), paired-end RNA-seq sequencing library was sequenced with a HiSeq xten/NovaSeq 6000 sequencer (2 × 150bp read length, Illumina, U.S.A). The raw paired end reads were trimmed and subjected to quality control by SeqPrep (https://github.com/jstjohn/SeqPrep) and Sickle (https://github.com/najoshi/sickle) with default parameters. Then clean reads were separately aligned to reference genome with orientation mode using the HISAT2 software (http://ccb.jhu.edu/software/hisat2/index.shtml). The mapped reads of each sample were assembled by StringTie (https://ccb.jhu.edu/software/stringtie/index.shtml? t = example) in a reference-based approach. To identify DEGs between two different samples, the expression level of each transcript was calculated according to the transcripts per million reads (TPM) method. RSEM (http://deweylab.biostat.wisc.edu/rsem/) was used to quantify gene abundances. Differential expression analysis was performed using the DESeq2 package with |log2FC|>1 and Q value ≤ 0.05 as the criteria of DEGs. GO functional enrichment and KEGG pathway analyses were carried out using Goatools (https://github.com/tanghaibao/Goatools) and KOBAS (http://kobas.cbi.pku.edu.cn/home.do) with Bonferroni-corrected p-value ≤0.05 considered to be the threshold of enrichment. The protein-protein interaction (PPI) network of selected DEGs was constructed using the STRING database [PMID: 30476243] and was mapped with Cytoscape software (v 3.8.2). An interaction score >0.4 was regarded as statistically significant.

2.16. Drosophila culture

Drosophila melanogaster (w1118) stocks were maintained and crossed according to standard laboratory procedures. Flies were raised under a 12/12 h, light/dark cycle at 25 °C with 60% humidity.

2.17. Measurement of total antioxidant capacity (TAC) in drosophila

Different groups of *Drosophila* were sacrificed and washed with PBS. 20 mg of tissue was suspended in ice cold PBS or HBSS (Hanks' Balanced

Salt Solution) and was thoroughly homogenized with an ultrasonic homogenizer. The tissue homogenates were centrifuged at 12,000 g and 4 °C for 5 min. The supernatant was collected for further experiments. The TAC in *Drosophila* after different treatments was determined *via* the ABTS•$^+$ assay with a test kit (Beyotime, China). Briefly, 20 μL peroxidase working solution, 10 μL supernatant of tissue homogenates, and 170 μL ABTS working solution were added in turn in a 96-well plate (one well per test) and were mixed gently. The mixture was incubated at room temperature for 6 min and then the absorbance (A_{test}) was measured at 414 nm. The TAC in the *Drosophila* group with the highest absorbance of ABTS•$^+$, which was the D-gal-treated group, was set as 0. And the TAC in other groups was calculated as ($A_{D-gal}-A_{test}$)/$A_{D-gal} \times 100\%$.

2.18. Determination of lifespan and climbing ability of drosophila

Newly eclosed wild-type female *Drosophila* were used for the lifespan assay. 100 flies were used for each group. Flies were transferred for fresh food and the death number was recorded every day. Data were presented as survival curves. For the climbing assay, eight male and eight female flies were placed in a plastic vial. The flies were gently knocked to the bottom of the vial before timing. Climbing distances within 4 s and 20 s were measured.

2.19. Statistical analysis

All quantitative data are shown as mean ± standard deviation in the figures. For determining the statistical significance of differences in the transcriptional levels of representative DEGs between the untreated and UPDA NPs-treated mouse kidneys, the likelihood ratio test included in the DEseq2 package of transcriptomics analysis was used. For evaluating the lifespan difference of *Drosophila* with different treatments, the log-rank test was used. For comparing the levels of specific parameters in different treatment groups, such as the expression of marker proteins, the biochemical indices and the behavioral performances, the one-way ANOVA (analysis of variance) with Tukey's *post hoc* test was used. The significance levels were set at $*p < 0.05$, $**p < 0.01$, $***p < 0.001$, and $****p < 0.0001$.

3. Results and discussion

3.1. Synthesis and characterization of UPDA NPs

The PDA nanoparticles (PDA NPs) were initially synthesized *via* oxidative self-polymerization of dopamine in alkaline solution (Fig. 2A), which showed very weak colloidal stability with the particle size ranging from the scale of nanometer to that of micrometer (Fig. 2B). The UPDA
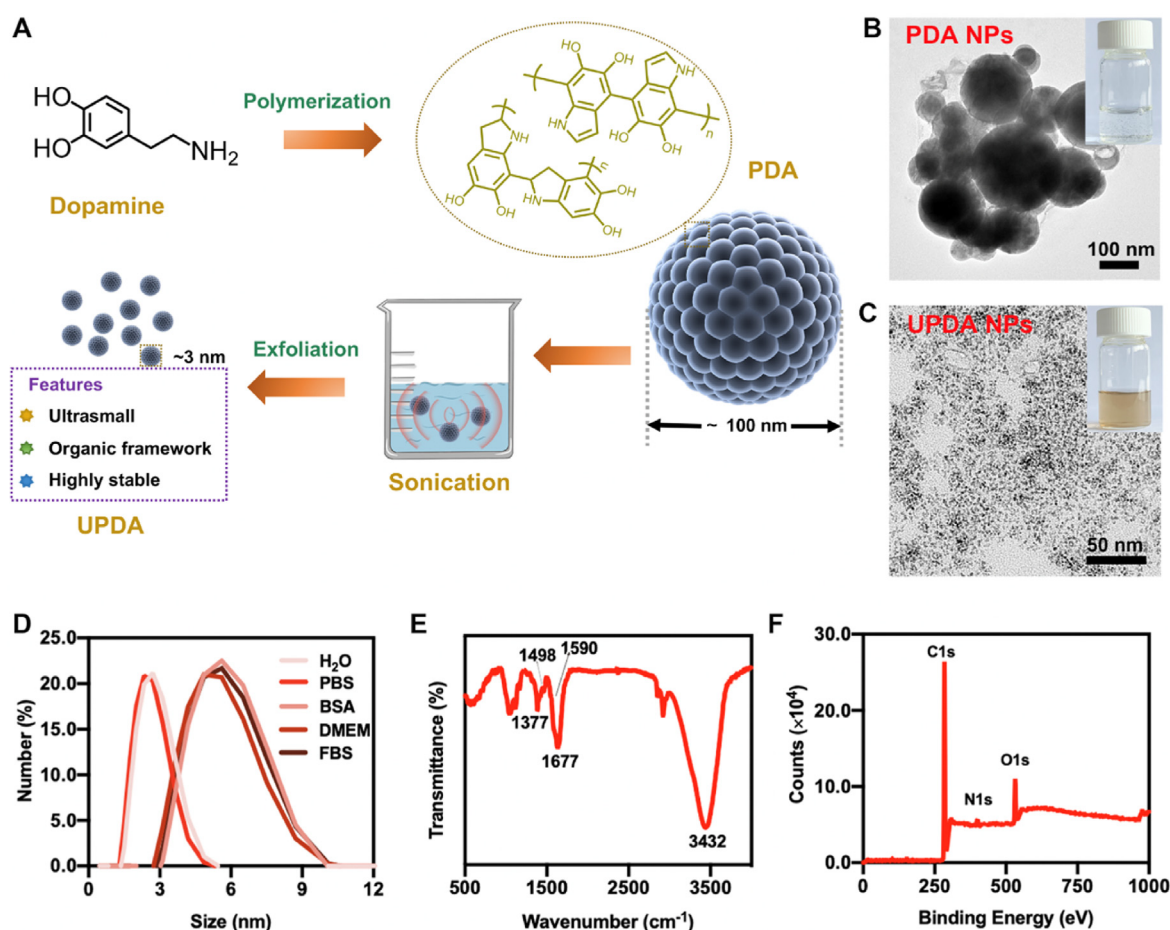
Fig. 2. The synthesis diagram and characterization of UPDA NPs. (A) The step-by-step production and key physical features of UPDA NPs. (B) A representative TEM image of PDA NPs. The inset is a representative photograph of PDA NPs dispersed in deionized water. (C) A representative TEM image of UPDA NPs. The inset is a representative photograph of UPDA NPs dispersed in deionized water. (D) DLS profiles of UPDA NPs dispersed in various solutions including deionized water, PBS, BSA, DMEM, and FBS. (E) The FT-IR spectrum of UPDA NPs. The functional groups O–H, N–H, and C–OH were identified. (F) The full-scale XPS spectrum of UPDA NPs. The C, N, and O elements were identified.

NPs can be facilely acquired from PDA NPs *via* ultrasonication-mediated liquid-phase exfoliation technique (Fig. 2A). Compared with PDA NPs, after exfoliation, the obtained UPDA NPs exhibited benign dispersity and stability (Fig. 2C). TEM images revealed the uniform size and morphology of UPDA NPs (Fig. 2C). The atomic force microscopy (AFM) image further demonstrated the successful synthesis of UPDA NPs with high quality and an average size of 3 nm (Fig. S1, Supporting information), which was consistent with what was observed in TEM images. The DLS analysis showed that the hydrodynamic diameter of UPDA NPs was 2.7, 2.4, 5.6, 4.9, and 5.2 nm in deionized water, PBS, BSA, FBS, and DMEM, respectively, and no obvious precipitation was observed after 72 h (Fig. S2, Supporting information), which indicates that UPDA NPs are relatively stable in various physiological environments and the size falls below the glomerular filtration size threshold of 6–8 nm (Fig. 2D) [36]. Furthermore, the functional groups of UPDA NPs were examined by utilizing an FT-IR spectrometer (Fig. 2E) with different adsorption bands indicating the presence of O–H, N–H, and C–OH, in which the adsorption band at ~ 3432 cm^{-1} is assigned to the stretching vibration of O–H and N–H, the peak located at ~ 1677 cm^{-1} is indexed to the stretching vibration of aromatic ring and the bending ring vibration of N–H, the peaks at ~ 1377 cm^{-1} and 1498 cm^{-1} are ascribed to the stretching and bending vibration of C–OH, and the peak at ~ 1590 cm^{-1} is assigned to the stretching vibration of the amide group, suggesting that UPDA NPs have been successfully synthesized [37]. UV–vis absorption spectra acquired on UPDA NPs displayed a broad and intense absorption band ranging from the ultraviolet region (100–400 nm) to the visible light region (400–700 nm) and the absorption was enhanced with the increased concentration of UPDA NPs, demonstrating excellent dispersity (Fig. S3, Supporting information). The X-ray powder diffraction (XRD) peak exhibited a bread-like pattern indicating the amorphous nature of UPDA NPs with intermolecular stacking structure (Fig. S4, Supporting information). Based on the XPS analysis, the C, N, and O elements are present in the acquired UPDA NPs (Fig. 2F and Fig. S5, Supporting information), further confirming the successful synthesis of UPDA NPs without residual by-products.

3.2. RONS-scavenging capability and SOD/CAT-like activity of UPDA NPs

The classic ABTS•$^+$ assay was performed to assess the TAC of UPDA NPs, in which ABTS•$^+$ is decolorized by antioxidants. The results showed that UPDA NPs had high antioxidant activity in a concentration-dependent manner (Fig. 3A), and more than 80% of total ROS could be eliminated by 40 µg mL^{-1} UPDA NPs (Fig. S6A, Supporting information). Significantly, the TAC of UPDA NPs is twice as much as that of 6-hydroxy-2,5,7,8-tetramethylchroman-2-carboxylic acid (Trolox), a water-soluble analog of vitamin E (Fig. S6B, Supporting information).

O$_2^{\bullet-}$, as the initial ROS, not only attacks unsaturated fatty acids causing lipid peroxidation, but also generates other oxygen free radicals through a series of reactions damaging organisms. SOD can catalyze O$_2^{\bullet-}$ into H$_2$O$_2$ and O$_2$, and thus SOD mimics can be used as a potential therapeutic agent against oxidative stress [13]. The SOD-like activity of UPDA NPs was initially assessed *via* the typical WST-1 method. O$_2^{\bullet-}$, generated from xanthine under the catalysis of xanthine oxidase, can react with WST-1, forming formazan with an absorption peak at 450 nm. The disproportionation of O$_2^{\bullet-}$ by SOD reduces the formation of formazan and thus SOD activity is negatively correlated with the absorbance of formazan. UPDA NPs efficiently inhibit the formazan generation with an IC$_{50}$ value of 39.98 µg mL^{-1}, suggesting a high SOD-like activity (Fig. 3B).

H$_2$O$_2$ is another kind of ROS that can induce numerous cellular events including cellular senescence. In living organisms, CAT collaborates with SOD to catalyze the decomposition of H$_2$O$_2$ into H$_2$O and O$_2$ for maintaining the redox homeostasis [38]. The CAT-like activity of UPDA NPs can be evaluated by detecting the change in the absorbance of H$_2$O$_2$ at 240 nm, which is an inherent characteristic of H$_2$O$_2$. In the presence of UPDA NPs, the absorbance value of H$_2$O$_2$ decreases significantly with time, indicating that UPDA NPs can effectively consume H$_2$O$_2$ (Fig. 3A,

Supporting information). Additionally, the ESR spin label oximetry was conducted to assess the CAT-like activity of UPDA NPs by monitoring the O$_2$ generation employing an oxygen-sensitive probe CTPO. There was a time-dependent decrease in the peak intensities of ESR signals (Fig. 3C), indicating continuous O$_2$ production. Furthermore, in an acidic environment, H$_2$O$_2$ can oxidize Fe^{2+} to Fe^{3+}, and Fe^{3+} combines with xylenol orange (XO) to form Fe^{3+} dye complexes. The complexes have a maximum absorption at 640 nm and the absorption value is proportional to the concentration of H$_2$O$_2$ [39]. Our results demonstrated that 84% of H$_2$O$_2$ was eliminated by using 50 µg mL^{-1} UPDA NPs (Fig. 3D and Fig. S7B, Supporting information). In order to clarify the catalytic mechanism of the CAT-like activity, a steady-state kinetic assay was conducted by adding H$_2$O$_2$ with different concentrations (5–60 µM) to 100 µg mL^{-1} UPDA NPs (Fig. 3E), which followed the representative Michaelis-Menten kinetics (Fig. 3F). By fitting a Lineweaver-Burk plot, the K_m and V_{max} values were calculated to be 87.0 µM and 1.5 µM s^{-1}, respectively (Fig. 3G).

•OH is one of the most reactive free radicals, which has stronger chemical reactivity and can dramatically aggravate oxidative damage [40]. MB was utilized as a chromogenic substance to demonstrate the •OH-scavenging effect of UPDA NPs. The blue-colored MB with a maximum absorbance at 664 nm turns colorless in the presence of •OH [41]. Our data demonstrated that UPDA NPs could effectively prevent the color fading of MB (Figs. 3H) and 75% of •OH was eliminated by 90 µg mL^{-1} UPDA NPs (Fig. S8, Supporting information). Moreover, 50 µg mL^{-1} UPDA NPs reduced the ESR signal of the •OH spin-trapped adduct DMPO to nearly the background level, indicating robust •OH-scavenging activity of UPDA NPs (Fig. 3I).

Besides ROS, RNS, whether endogenous or exogenous, can induce cellular oxidative damage and further cause senescence [42]. The total RNS-scavenging activity of UPDA NPs was examined based on the elimination test of DPPH•, which is a stable nitrogen free radical with a large number of unpaired electrons [38] and a colorimetric probe with a strong absorption at 532 nm. The nitrogen lone pair electrons can be combined by RNS scavengers and the corresponding absorption is consequently weakened. Our results revealed that UPDA NPs could effectively eliminate DPPH• in a concentration-dependent manner (Fig. 3J). Approximately 85% of DPPH• was quenched by 100 µg mL^{-1} UPDA NPs (Fig. S9, Supporting information).

Among RNS, excessive •NO can cause cytotoxicity and accelerate aging [43]. The •NO-scavenging activity of UPDA NPs was assessed by using carboxy-PTIO as the •NO indicator, and NOC 18 as the •NO donor [44]. Carboxy-PTIO alone presents 5 peaks of ESR signal and can react with •NO to generate carboxy-PTI and nitrogen dioxide radical (•NO$_2$), resulting in an increase of ESR signal from 5 to 7 peaks. When UPDA NPs were added, the ESR signal was restored to 5 peaks (Fig. 3K), indicating the clearance of •NO.

O$_2^{\bullet-}$ can react with •NO resulting in the formation of ONOO$^-$, which is a highly oxidative and cytotoxic factor. Pyrogallol red with an absorbance peak at 545 nm has been commonly used for quantifying ONOO$^-$ [45]. The bleaching of pyrogallol red by ONOO$^-$ was substantially inhibited by UPDA NPs and 88% of ONOO- was scavenged by 100 µg mL^{-1} UPDA NPs (Fig. 3L and Fig. S10, Supporting information). Taken together, all these results demonstrate that UPDA NPs possess outstanding RONS-scavenging abilities.

In terms of chemical structures and functionalities, PDA is very similar to eumelanin, the most common form of melanin [46]. In eumelanin, for scavenging RONS, the intermolecular connections between 5,6-dihydroxyindole-2-carboxylic acid (DHICA) oligomers can distort the dihedral angles between rings to minimize electrostatic interactions. The stacking difficulties of oligomers cause the delocalization of π electrons and the weak intermolecular aggregation makes it easier for radicals to access DHICA, providing strong antioxidant capacity [47]. Similarly, as a eumelanin-like agent, the free radical-scavenging property of PDA is principally contributed by the degree of electron delocalization in the plane of the oligomers (Fig. 3M), which is related to the reactivity
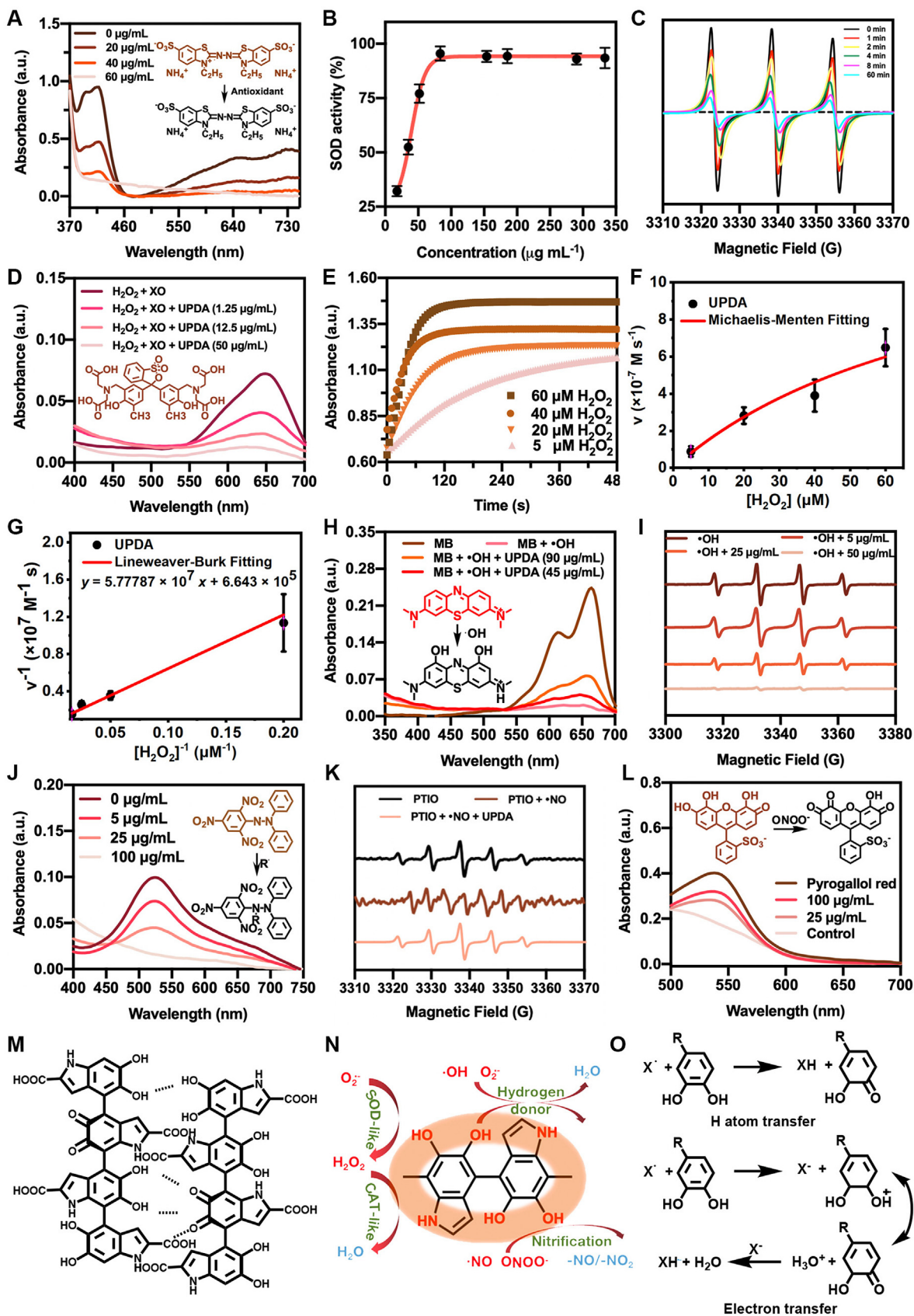
(caption on next page)

Fig. 3. The multiple RONS-scavenging effects of UPDA NPs and the underlying mechanism. (A) TAC of UPDA NPs represented by the absorbance reduction of radical cation ABTS•+. The antioxidant activity of UPDA NPs enhances with its concentration increasing. (B) SOD-like activity of UPDA NPs represented by the percentage reduction of formazan formation. $O_2^{\bullet-}$ reacts with WST-1, generating formazan with an absorption peak at 450 nm. (C) ESR spectra of CTPO demonstrating time-dependent O_2 production from H_2O_2 decomposition by UPDA NPs (50 μg mL^{-1}). CTPO is an O_2-sensitive probe. (D) CAT-like activity of UPDA NPs represented by the absorbance reduction of Fe^{3+}-XO complex at 640 nm. The Fe^{3+} comes from the oxidation of Fe^{2+} by H_2O_2. (E) Absorbance of Fe^{3+}-XO complex upon the addition of 100 μg mL^{-1} UPDA NPs to varied concentrations of H_2O_2. (F) Michaelis-Menten curve and (G) Lineweaver-Burk plot of CAT-like activity of UPDA NPs. (H) •OH-scavenging ability of UPDA NPs represented by the absorbance increase of MB. UPDA NPs prevents the degradation of MB by •OH. (I) ESR spectra of DMPO demonstrating the concentration-dependent •OH-scavenging effect of UPDA NPs. (J) Total RNS-scavenging ability of UPDA NPs represented by the absorbance reduction of DPPH•. (K) ESR spectra of PTIO demonstrating the •NO-scavenging ability of UPDA NPs. The ESR signal of carboxy-PTIO is represented by 5 peaks. Carboxy-PTIO reacts with ·NO, generating carboxy-PTI and •NO$_2$, which increases the ESR signal to 7 peaks. UPDA UPs capture ·NO and reduce the ESR signal to the original 5 peaks. (L) ONOO$^-$-scavenging ability of UPDA NPs represented by the absorbance increase of pyrogallol red. (M) π electronic delocalization of PDA particles. (N) Schematic diagram of UPDA NPs donating hydrogen atoms with surface-active groups. (O) The free radical-scavenging mechanism of UPDA NPs with catechol being the core functional group. (For interpretation of the references to colour in this figure legend, the reader is referred to the Web version of this article.)

---

of polycatechol structure on the surface and the intrinsic lifetime of the inner radicals [48]. In addition, the ultrafast energy transfer facilitated by ion binding is another way for melanin to quench chemically active molecules [49]. It can be speculated that the typical redox chemistry of catechols endows UPDA NPs with the function of scavenging various free radicals (Fig. 3N). On the one hand, the catechol provides hydrogen atoms from phenolic hydroxyl groups to quench RONS free radicals. On the other hand, catechol can also reduce RONS *via* electron transfer, and the resulting phenoxy radicals further form a stable quinone structure by interacting with a second radical (Fig. 3O) [50,51].

3.3. UPDA NPs suppress oxidative stress-induced senescence in vitro

As for the effects of UPDA NPs in senescent cells, we hypothesize that external pressures and stimuli induce cellular senescence resulting in the secretion of factors related to the SASP, which may further lead to the accumulation of more senescent cells, and UPDA NPs, as an RONS scavenger, can delay or even reverse this process by intervening in this cycle to regain a healthy loop that prevents senescent cells from accumulating and restores cellular homeostasis (Fig. 4A). To verify this hypothesis, human embryonic kidney epithelial 293 T cell line was selected for further evaluation. Our results showed that UPDA NPs did not induce obvious cytotoxicity and the survival rate of 293 T cells was above 80% even when treated with 200 μg mL^{-1} UPDA NPs (Fig. S11, Supporting information). DOX, an anthracycline antibiotic extensively and effectively utilized against a broad range of cancers, can also serve as an inducer of cellular senescence [52]. And D-gal has been generally applied as an inducer to accelerate aging as shown before [53]. Similar to H_2O_2-treated cells, an increase in ROS level shown by DCF was exhibited in cell groups after DOX or D-gal incubation (Fig. 4B and Fig. S12, Supporting information). Distinctly, UPDA NPs effectively decreased the ROS generation caused by H_2O_2, DOX or D-gal, and thus protected 293 T cells from ROS-induced cytotoxicity (Fig. 4B and Fig. S12, Supporting information). Quantitative analysis of intracellular ROS levels *via* flow cytometry further confirmed that UPDA NPs even at a low concentration of 20 μg mL^{-1} possessed the desirable capability to protect the cells against DOX-induced oxidative stress (Fig. 4C).

Senescence is commonly accompanied by an increase in the activity of senescence-associated β-galactosidase (SA-β-GAL) [54]. As expected, we found that SA-β-GAL expression elevated with the concentration of DOX increasing and the cell number began to decrease when the concentration of DOX exceeded 0.2×10^{-6} M (Fig. S13, Supporting information). It has been reported that senescence-related cell cycle arrest is activated by p16^{INK4A}/pRB and/or p53/p21$^{WAF1/CIP1}$ tumor suppressor pathways [7]. p16^{INK4A} is a key player in oncogene-induced senescence and has been shown to promote tissue aging and inflammation [55,56]. We found a notable increase of p16^{ink4a} expression after DOX stimulation, whereas UPDA NPs effectively diminished this effect (Fig. 4D–G). The upregulation of cyclin-dependent kinase inhibitor p21 and its transcription activator p53 are thought to be involved in senescence-related diseases [57]. Besides, another senescence mediator, DcR2, has been shown to be related to the premature senescence involved in kidney

fibrosis [58]. Our western blotting results revealed that p21 and DcR2 were overexpressed in DOX-treated 293 T. Strikingly, after UPDA NPs treatment, the protein levels of both p21 and DcR2 decreased (Fig. 4J and K). Moreover, the interaction between transcription factor FOXO4 and p53 is considered as a potential target for developing treatment strategies for age-related illnesses [59]. Similar to the aforementioned senescence markers, the expression of FOXO4 was boosted by DOX, while this effect was diminished by UPDA NPs (Fig. 4D and E). Furthermore, the levels of SASP cytokines interleukin-1β (IL-1β) and interleukin-6 (IL-6) were quantified using enzyme-linked immunosorbent assay (ELISA) kits, which demonstrated that UPDA NPs could significantly downregulate their expression in senescent 293 T cells (Fig. 4H and I). Interestingly, the expression level of nuclear lamin protein lamin B1, a protein crucial to maintain the structural integrity of the nucleus, which is impaired at the beginning of senescence [60] and therefore the loss of which is seen as a senescence marker [61], was restored following UPDA NPs treatment in DOX-induced senescent cells (Fig. 4D, F, J, K).

3.4. Biocompatibility and biosafety assessment of UPDA NPs in vivo

To explore the therapeutic effects of UPDA NPs *in vivo*, we firstly evaluated their biocompatibility and biosafety in mice. There was no necrosis, congestion or bleeding in the main organ tissues including the heart, the liver, the spleen, the lung, and the kidney after intravenous injection of UPDA NPs at a dose of 2 mg/kg, revealing no adverse effects (Fig. S14, Supporting information). The crucial hematological parameters, including WBC, LYM, MON, GRA, MPV, RBC, HGB, MCH, HCT, RDWSD, MCV, MCHC, PLT, PDW and RDWCV, had no significant differences between the control group and UPDA NPs-treated group (Fig. 5B-P), indicating that UPDA NPs possess benign biocompatibility and high biosafety. Moreover, the inherent brownish yellow color of UPDA NPs makes them directly visible in the bladder (Fig. S15, Supporting information), which confirms that UPDA NPs are eventually cleared from the kidney through urine excretion.

3.5. UPDA NPs display anti-aging effects in vivo

Based on the robust RONS-scavenging ability and biosecurity of UPDA NPs, we evaluated the physiological and physical functions of DOX-induced aging mice (Fig. 5A). Compared with the control group, the levels of conventional indicators of renal and hepatic functions, CRE, BUN, ALT, and AST, elevated in DOX-exposed mouse group (Fig. 5B–E), indicating that DOX triggers kidney and liver damage. In contrast, after UPDA NPs treatment, these parameters returned to their normal levels, demonstrating the protective effects of UPDA NPs for the kidney and the liver. To further assess the treatment efficacy of UPDA NPs, the swimming behaviors of mice were tracked and evaluated (Fig. 5F). Our results showed that the average swimming speed of DOX-treated mice was measured to be 123.36 mm s^{-1}. Interestingly, after UPDA NPs treatment, the DOX-treated mice exhibited an enhanced swimming ability with a higher average swimming speed (212.86 mm s^{-1}). Furthermore, the body weight of DOX-treated mice displayed an apparent decrease, which
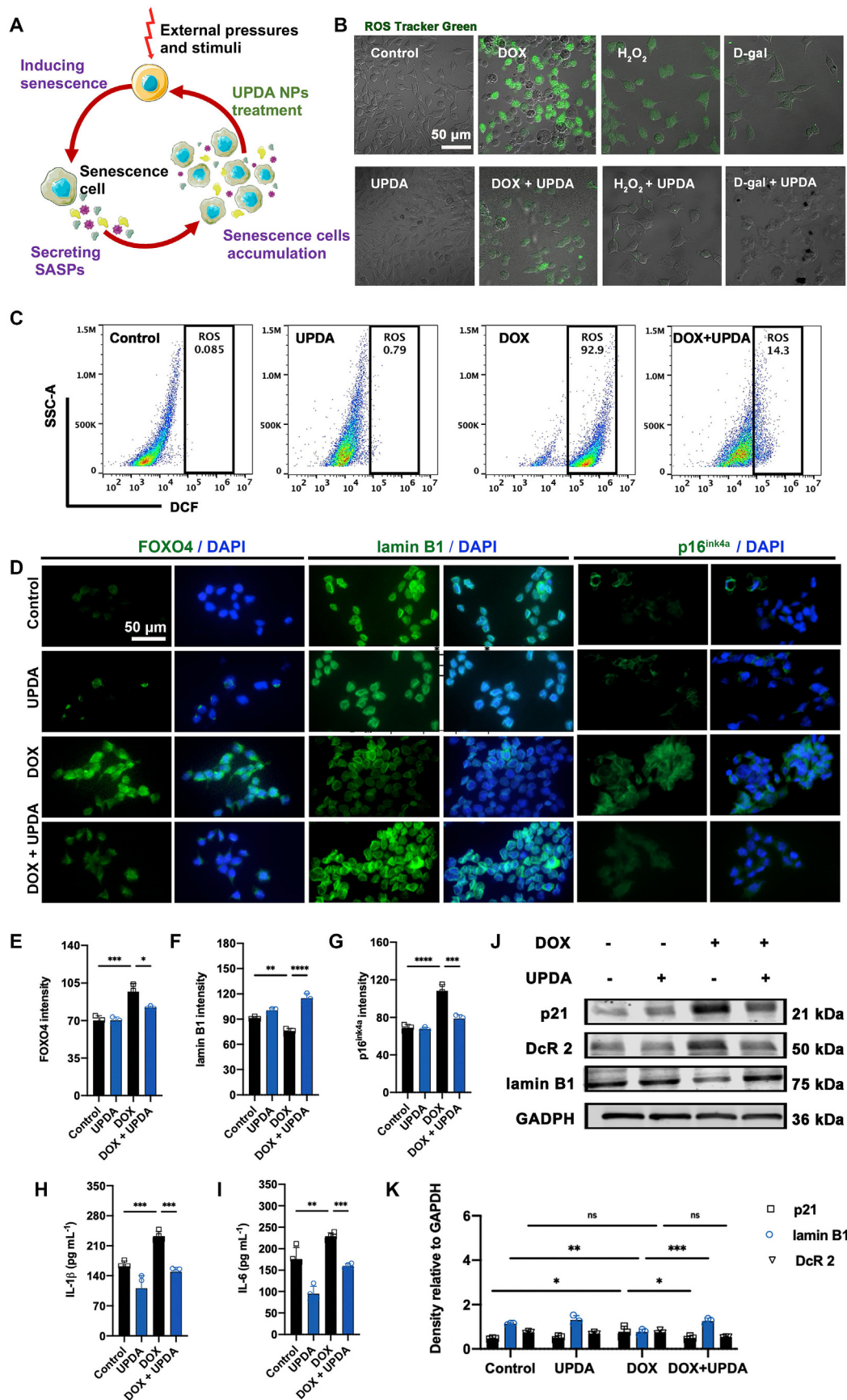
(caption on next page)

Fig. 4. UPDA NPs attenuate oxidative stress-induced cellular senescence *in vitro*. (A) Hypothesis of the effects of UPDA NPs in senescent cells. (B) ROS levels indicated by the green fluorescence of DCF in 293 T cells incubated with DOX, H_2O_2, D-gal, UPDA NPs, DOX + UPDA NPs, H_2O_2+UPDA NPs, or D-gal + UPDA NPs. (C) Flow cytometric analysis of ROS levels represented by DCF fluorescence in 293 T cells after different treatments. (D) Representative confocal microscopy images of FOXO4, lamin B1, and p16^{ink4a} in 293 T cells after different treatments. (E–G) Quantification of fluorescence intensities of immunolabeling for FOXO4, lamin B1, and p16^{ink4a} in different cell groups represented by (D). (H, I) ELISA quantification of IL-1β and IL-6 in 293 T cells after different treatments. (J) Representative western blots of p21, DcR2, and lamin B1 in 293 T cells after different treatments. GADPH was used as a loading control. (K) Densitometric analysis of p21, DcR2, and lamin B1 in different cell groups represented by (J). The absolute intensities of protein bands on western blots were measured and normalized against those of GAPDH to obtain relative intensities. For (A-I, K), the untreated cell group is the control. For (B, E-I, K), n = 3 batches of cells, *p < 0.05, **p < 0.01, ***p < 0.001, and ****p < 0.0001 using one-way ANOVA with Tukey's *post hoc* test. (For interpretation of the references to colour in this figure legend, the reader is referred to the Web version of this article.)
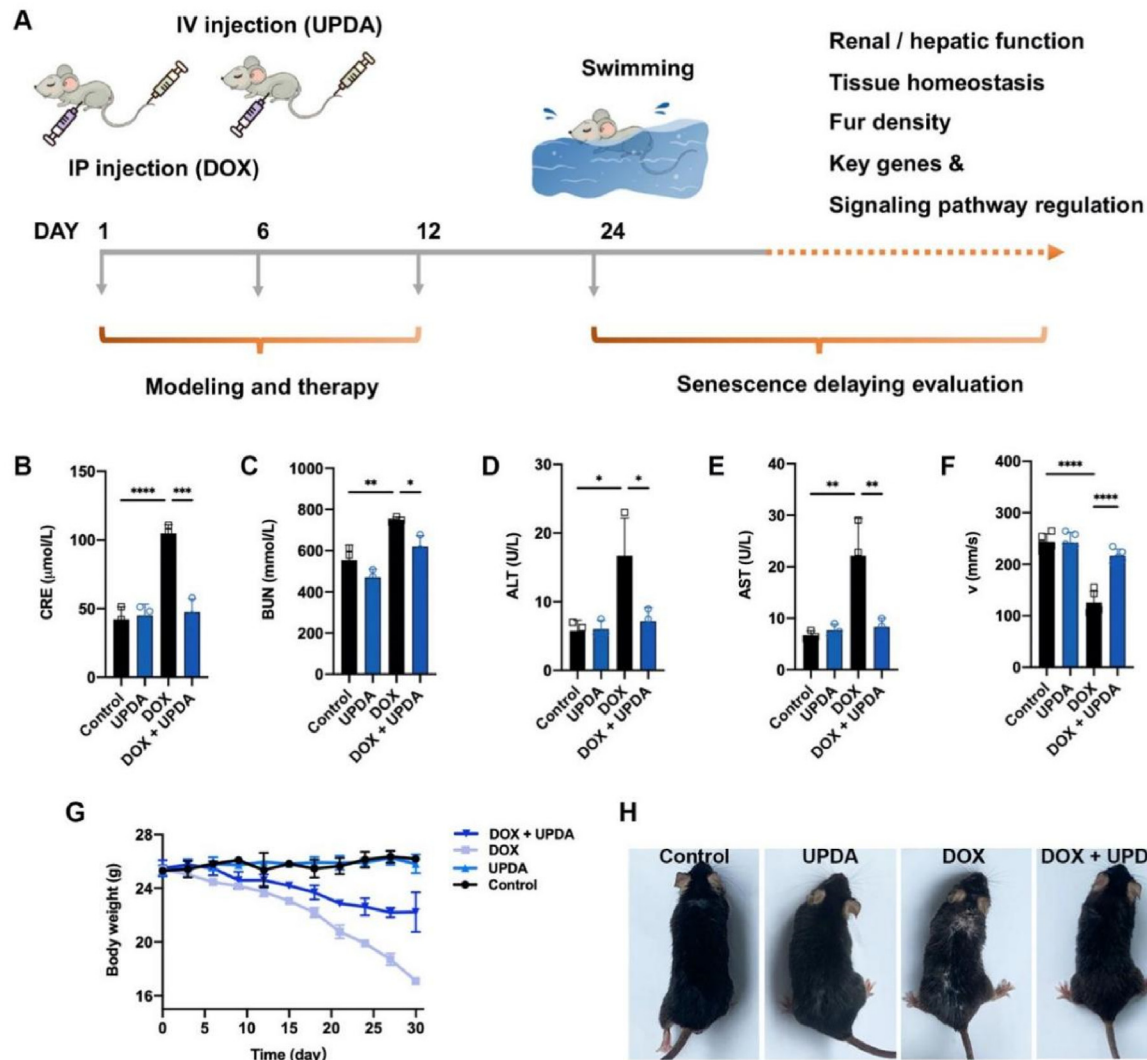
Fig. 5. The alleviating effects of UPDA NPs on DOX-induced senescence in mice shown by the evaluation of physiological indicators and physical performances. (A) Schematic depiction of the procedure for UPDA NPs administration and tests in DOX-treated mice. (B, C) Serum levels of kidney function indicators CRE and BUN in mice after different treatments. (D, E) Serum levels of liver function indicators ALT and AST in mice after different treatments. (F) The average swimming speeds of mice after different treatments. (G) Weight changes of mice after different treatments. (H) Representative fur appearances of mice receiving different treatments. The control mice were injected with PBS. For (B-E, G), n = 3 mice/group. For (F), n = 5 mice/group. For (B–F), *p < 0.05, **p < 0.01, ***p < 0.001, and ****p < 0.0001 using one-way ANOVA with Tukey's *post hoc* test. For (H), a cohort of at least 5 mice in each group were observed and compared.

was significantly ameliorated by UPDA NPs (Fig. 5G). In the aging phenotype evaluation, age-related hair loss was clearly observed in DOX-treated mice, whereas there was a significant increase in the hair density of DOX-treated mice following UPDA NPs treatment (Fig. 5H), further demonstrating the anti-senescence effects of UPDA NPs.

Next, the key players involved in the activation of senescence-related signaling pathway were assessed following the treatment of UPDA NPs.

We found that the expression of both p21 and p53 in mouse kidney was upregulated after DOX treatment, while their levels were significantly decreased after UPDA NPs treatment (Fig. 6A, B, D). Moreover, consistent with our results *in vitro*, lamin B1 expression was attenuated by DOX, which was obviously restored after UPDA NPs treatment (Fig. 6A, C). Thus, our results suggest that UPDA NPs may participate in preventing the onset of aging.
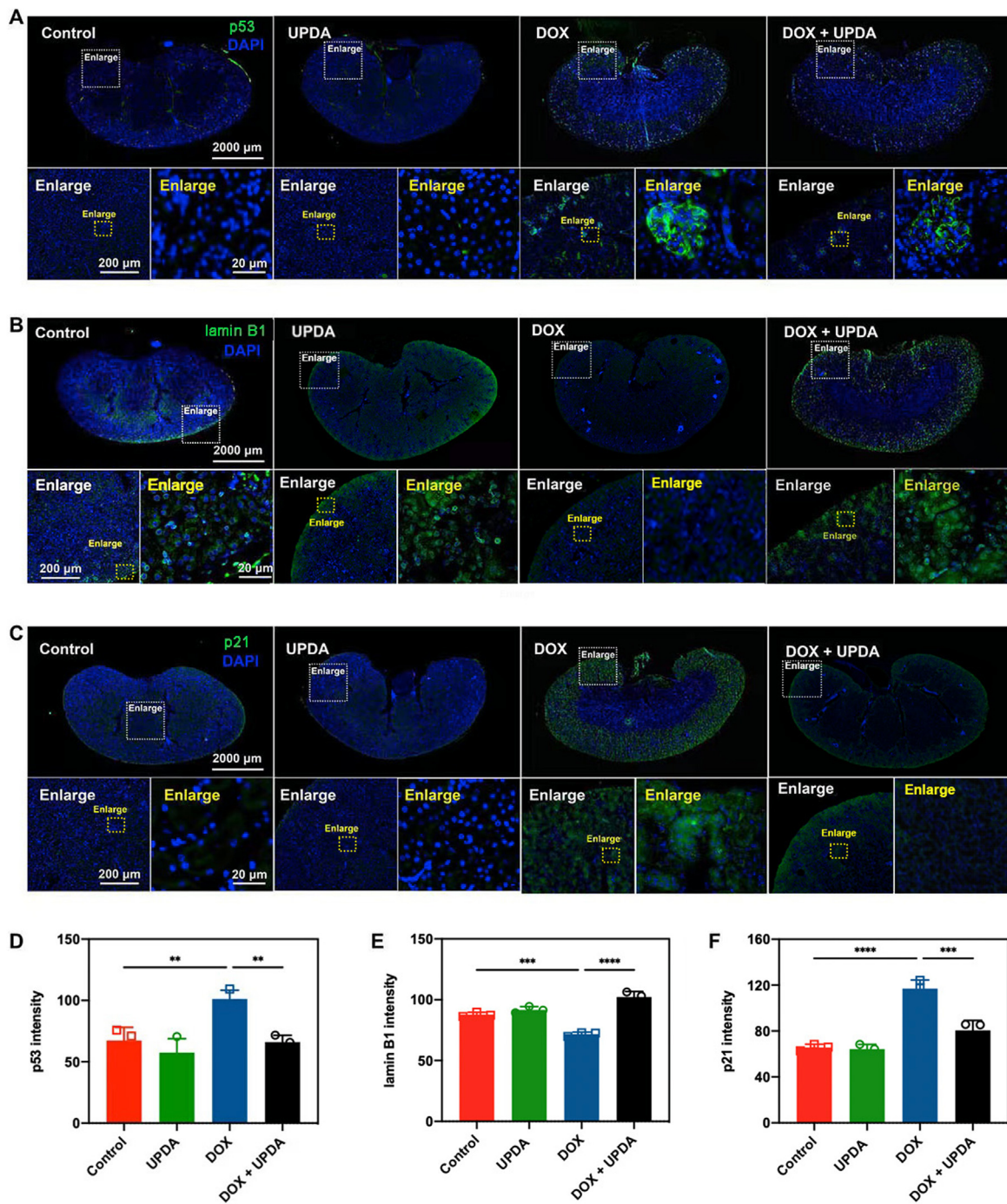
Fig. 6. Evaluation of renal senescence in mice and the anti-aging effects of UPDA NPs. (A–C) Representative confocal microscopy images of kidney sections of mice treated with PBS (control), UPDA NPs, DOX or DOX + UPDA NPs for the fluorescent labeling of p53, lamin B1, and p21. (D–F) Quantification of fluorescence intensities of immunolabeling for p53, lamin B1, and p21 in kidney sections from different mouse groups represented by (A–C). For (D–F), n = 3 mice/group, **p < 0.01 and ****p < 0.0001 using one-way ANOVA with Tukey's *post hoc* test.

3.6. UPDA NPs regulate gene expression related to multiple biological functions

To elucidate the underlying mechanisms of UPDA NPs against oxidative stress-induced senescence, we performed transcriptomics analysis on the kidneys of mice treated with DOX. An unsupervised principal component analysis (PCA) revealed that there was a significant difference in the transcriptomic profile of the kidney between the untreated group and UPDA NPs-treated group (Fig. 7A). As shown in the volcano plot, 960 DEGs (Fig. 7B) were identified, including 474

upregulated DEGs and 486 downregulated DEGs. It is noticed that the networks of DEGs are enriched in multiple signaling pathways shown by Kyoto Encyclopedia of Genes and Genomes (KEGG) analysis, with pathways of cytokine-cytokine receptor interaction topping the chart (Fig. 7C). This is in accordance with our observation that the levels of SASP cytokines IL-6 and IL-1β could be regulated by UPDA NPs.

As expected, the functions of UPDA NPs-regulated DEGs are mostly enriched in the pools associated with aging and oxidative stress shown by Gene Ontology (GO) analysis (Fig. 7D). We then further confirmed the identities of these DEGs to predict the cellular activities that UPDA NPs
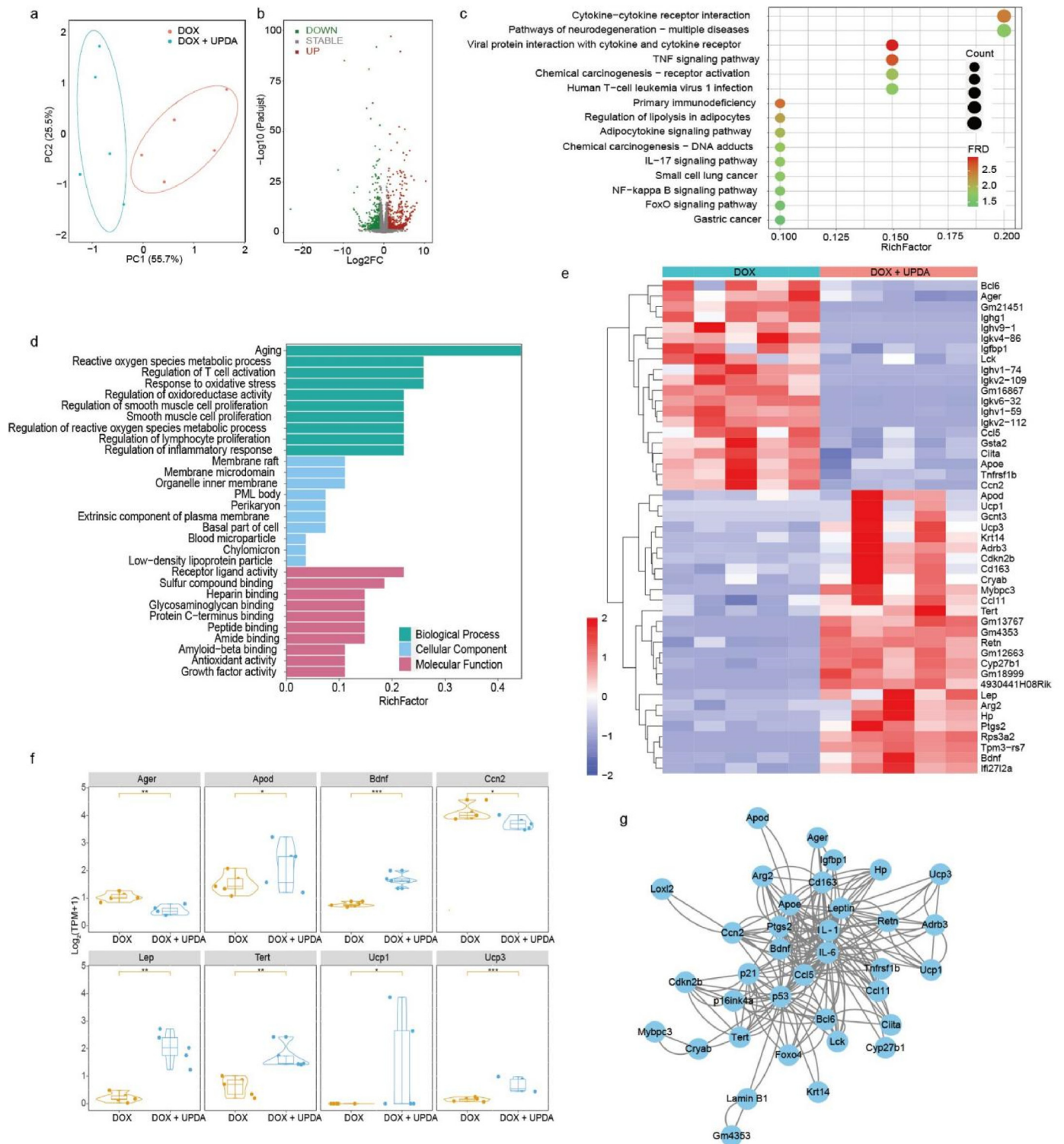
Fig. 7. Transcriptomics and functional enrichment analyses of DEGs in the kidneys of DOX-treated mice without or with the administration of UPDA NPs. (A) PCA map of DEGs in the kidneys of DOX-induced mice without or with UPDA NPs treatment. Each data point corresponds to the PCA analysis of an independent sample. (B) Volcano plot showing the upregulated, downregulated, and unregulated gene clusters in the kidneys of DOX-induced mice after UPDA NPs treatments. (C) KEGG pathway enrichment analysis and (D) GO analysis of DEGs in the kidneys of DOX-induced mice following UPDA NPs treatment. (E) Heat map of DEGs in gene categories related to oxidative stress and aging. (F) Box plots of representative DEGs (Ager, Apod, Bdnf, Ccn2, Lep, Tert, Ucp1, and Ucp3) in the kidneys of DOX-induced mice without or with UPDA NPs treatment (n = 5 mice/group, *p < 0.05, **p < 0.01, and ***p < 0.001 using likelihood ratio test). (G) The PPI network of oxidative stress and aging-associated DEGs regulated by UPDA NPs. An interaction score >0.4 was considered to be statistically significant.

might be involved in (Fig. 7E). Among the upregulated DEGs (Fig. 7F), we found genes important in diverse biological processes. ApoD (apolipoprotein D), a lipocalin mainly expressed in the nervous system, is believed to restrain lipid peroxidation and act against oxidative stress in the brain [62]. Ucp1 (uncoupling protein 1), a biomarker of the brown adipose tissue, has reduced expression and activity during aging [63]. While Ucp1 deficiency leads to the overproduction of mitochondrial superoxide and vascular inflammation, Ucp1 knockin in pigs prevents NLRP3 inflammasome activation and protects the animals against coronary atherosclerosis [64]. Another UPDA NPs-upregulated uncoupling

protein Ucp3 is a negative regulator of mitochondrial ROS generation and has protective effects against oxidative stress in skeletal muscle and heart [65]. Tert (telomerase reverse transcriptase), the catalytic subunit of telomerase is a generally recognized inhibitor of cellular senescence [66]. Acute administration of leptin (lep), a key hormone in the maintenance of energy homeostasis, can reduce oxidative stress levels by suppressing superoxide generation and promote cell proliferation in the brain of an Alzheimer's disease mouse model [67]. Bdnf (brain-derived neurotrophic factor), a neurotrophin essential for neuronal survival and synaptic transmission, has been shown to maintain redox balance in
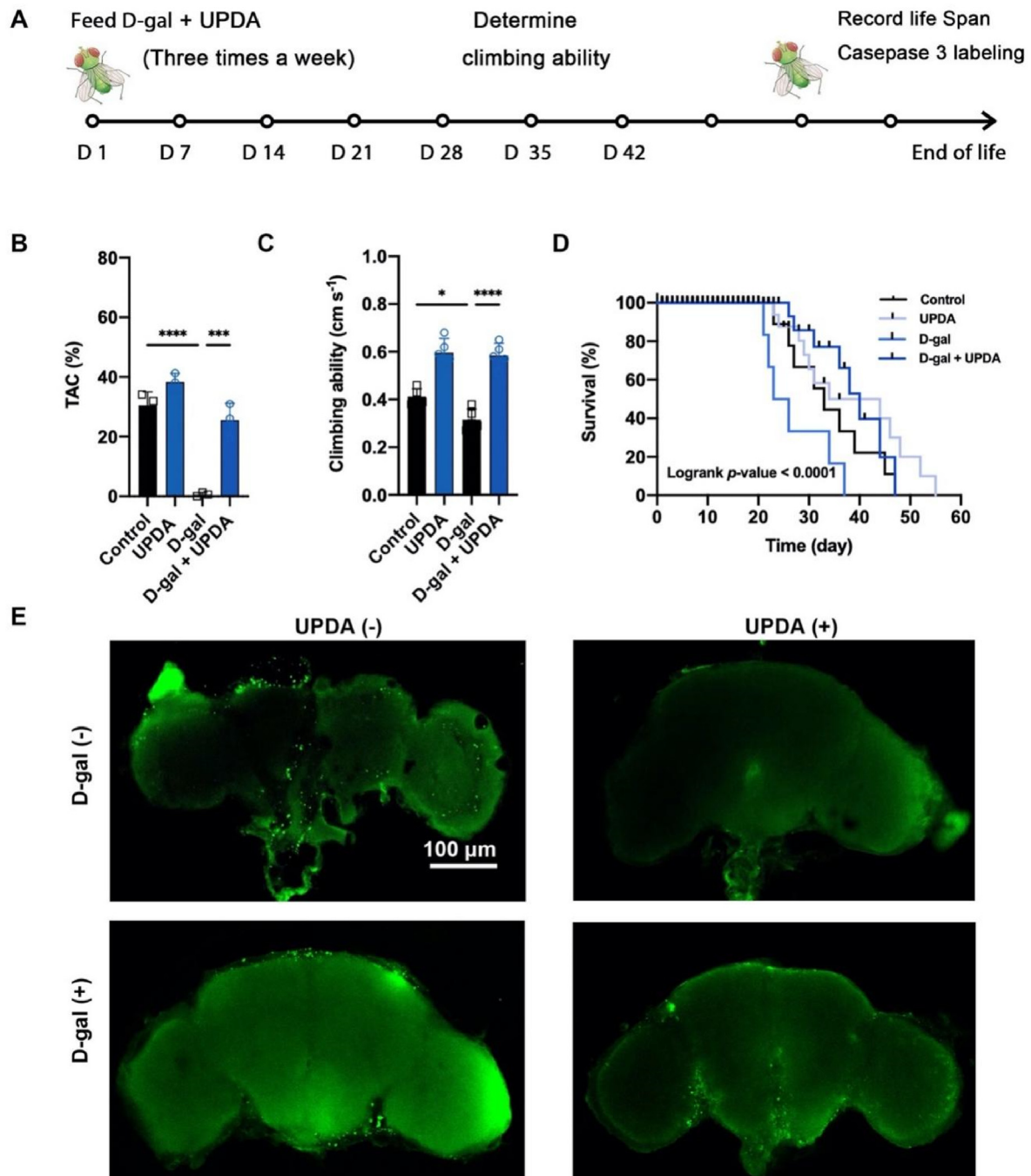
Fig. 8. The reversing effects of dietary UPDA NPs on the senescence of *Drosophila* induced by D-gal. (A) Schematic illustration of the procedure for UPDA NPs administration and tests in D-gal treated *Drosophila*. (B) The TAC in *Drosophila* after different treatments represented by the proportion of absorbance reduction of ABTS•[+]. (C) Climbing abilities of 35-day-old *Drosophila* after different treatments. (D) Survival rates of *Drosophila* after different treatments. (E) Apoptosis detection using caspase-3 immunofluorescence staining in the brain of *Drosophila* after different treatments. For (B, C), n = 16 flies/group, *p < 0.05, ***p < 0.001, and ****p < 0.0001 using one-way ANOVA with Tukey's *post hoc* test. For (D), n = 100 flies/group, p < 0.0001 using the long-rank test.

neuronal cultures [68] and reverse microglial activation in aged mice *via* the inhibition of NF-κB activity [69]. The up-regulation of these aging-sensitive genes indicates that the treatment by UPDA NPs can activate multiple pathways against oxidative stress-induced renal senescence and the consequent antioxidation effects may also play a part in the protection of other major organs apart from the kidney, such as the brain, the muscle and the heart. Particularly, the NF-κB signaling pathway, a fundamental stimulator of SASP [70], was identified as one of the enriched pathways of UPDA NPs-regulated DEGs. Correspondingly, in the pool of downregulated DEGs (Fig. 7F), Arger (advanced glycosylation end product-specific receptor), also known as receptor for advanced glycation end products (RAGE), can activate NF-κB signaling pathway, which in turn leads to inflammation [71]. Another downregulated gene Ccn2 (cellular communication network factor 2) is found to enhance NF-κB signaling by binding to a receptor activator of NF-κB (RANK) [72]. Additionally, we took advantage of the Search Tool for the Retrieval of Interacting Genes (STRING) to obtain the PPI network for the DEGs related to aging and oxidative stress. Several hub genes were identified, including p16[ink4a], p21, p53, IL-1β, and IL-6 (Fig. 7G), the expression of which can be suppressed by UPDA NPs. Furthermore, NF-κB signaling pathway can be activated by an array of stimuli, including proinflammatory cytokines IL-6 and IL-1β [73]. Therefore, our results imply that the antioxidant activity of UPDA NPs combines multiple mechanisms against senescence, including the anti-inflammatory regulation through the suppression of NF-κB signaling pathway.

3.7. Dietary UPDA NPs delay aging in drosophila

Due to the low culture cost, high reproductive rate, and short generation time and lifespan, *Drosophila* has been used as a model organism in senescence research for a long time [74]. We examined the effects of dietary UPDA NPs on the senescence and lifespan in *Drosophila* (Fig. 8A). As expected, the TAC in *Drosophila* shown by the ABTS•[+] scavenging activity was diminished by D-gal, while dietary UPDA NPs could significantly recover D-gal-induced TAC loss (Fig. 8B). The climbing ability of D-gal-fed *Drosophila* was significantly improved after UPDA NPs treatment. Specifically, the average climbing speed of D-gal treated *Drosophila* was about 0.37 cm s^{-1}, which was increased to 0.58 cm s^{-1} by dietary UPDA NPs (Fig. 8C). Additionally, while D-gal forcefully shortened the maximum longevity of *Drosophila* to 37 days, UPDA NPs feeding could prolong the maximum life span of D-gal-treated *Drosophila* to 46 days, identical to that of the control group (Fig. 8D). Interestingly, UPDA NPs alone could further increase the maximum life span of untreated *Drosophila* to 55 days. The immunostaining of caspase-3 was performed to visualize the apoptosis in the brain of *Drosophila* (Fig. 8E), demonstrating that UPDA NPs obviously inhibited D-gal-caused cell death. Taken together, our results indicate that UPDA NPs may play an important role in protecting *Drosophila* from aging.

4. Conclusions

In the present study, we focused on eliminating one of the key contributors for senescence, the RONS, by means of biocompatible nanomedicine. Since dopamine is a natural antioxidant and its polymer PDA is a widely used biomaterial in the medical field, we developed UPDA NPs to further explore their therapeutic potentials for senescence.

UPDA NPs not only exhibit CAT/SOD mimetic activities with a wide range of ROS-scavenging capabilities but are also effective in removing RNS such as •NO and ONOO$^-$. We speculate that the radical-scavenging properties of UPDA NPs are attributed to the catechol groups in their chemical structure, which can capture RONS free radicals through a dual effect of hydrogen atom transfer and electron transfer. Also, the ultrasmall size of UPDA NPs grants expanded contact area with free radicals, and therefore the anti-aging effect is greatly enhanced compared to nanoparticles of larger sizes.

Our UPDA NPs are proven to be safe and biocompatible *in vivo*, which

verifies their potentials for clinical translation. The RONS-scavenging effects of UPDA NPs are highly efficient in preventing or reverting senescence, as demonstrated in our senescent models both *in vitro* and *in vivo*. This is associated with the modulation of genes related to SASP, including p16[INK4A], p21, p53, FOXO4, lamin B1, and DcR2. UPDA NPs are able to inhibit the expression of p16[INK4A], p53, and p21, which is in line with a study showing the anti-aging mechanism of gold nanoparticles [75]. Particularly, the therapeutic potentials of UPDA NPs in the treatment of senescence are confirmed by the improvements of senescent phenotypes and behavioral performances of accelerated aging mice. We showed that UPDA NPs could restore the fitness, the fur density, and the renal function in DOX-induced senescent mice, similar to the effects of a FOXO4 peptide interfering in FOXO4-p53 interaction for the treatment of fast aging mice [51]. Collectively, our results demonstrate that UPDA NPs have great potential for alleviating and reversing oxidative stress-induced aging *via* the regulation of SASP-related molecules.

Our *in vitro* and *in vivo* studies support multiple anti-aging mechanisms of UPDA NPs, as these particles are also capable of regulating the expression of the hub genes (p16[INK4A], p21, p53, IL-6, and IL-1β) in the protein-protein interactome of DEGs. Remarkably, UPDA NPs can increase the antioxidant capacity, enhance the climbing ability, and extend the lifespan of senescent *Drosophila*, which is likely to be associated with the prevention of apoptosis in the brain. Since apoptosis *per se* can be induced by multiple factors, such as cell cycle inhibitor p16[INK4A] [76] and proinflammatory cytokine IL-1β [77], the anti-senescence effects of UPDA NPs may derive from a combination of different mechanisms against aging and are worthy of further investigation.

In summary, we have engineered a uniform and stable organic polymer-based nanozyme UPDA NPs that exhibit extensive RONS-eliminating capacities and anti-senescence potentials. Although we have verified the antioxidant properties of UPDA NPs by revealing their cytoprotective and anti-aging effects in drug-induced senescent cells and model organisms, there are further validations required before UPDA NPs are put into use clinically. For example, it would further confirm the prospect of using UPDA NPs for the treatment of senescence if our results could be repeated in natural aging models and aging-related disease models. To accelerate the clinical translation of UPDA NPs, we propose future studies as follows: compare different administration approaches of UPDA NPs and identify the optimum delivery method; evaluate the anti-aging effects of UPDA NPs in the senescence-accelerated mouse (SAM) model [78], a progeria syndrome mouse model [79] and a mouse model for Alzheimer's disease [80]; assess the anti-aging effects of UPDA NPs using samples (cells and tissues) collected from elderly individuals and patients suffering from aging-associated diseases. We expect that UPDA NPs-enabled antioxidation may provide further insights into the application of organic nanomedicine in the treatment of premature senescence and senescence-related diseases.

Credit author statement

Jiamei Han: Experiment, Writing-Original Draft, Validation, Formal analysis, Visualization, Software, Methodology, Data curation. Jiao Wang: Resource, Methodology. Hongwei Shi: Experiment, Methodology. Qian Li: Writing-Review&Editing. Shibo Zhang: Experiment, Methodology. Hao Wu: Data curation, Methodology. Wenjun Li: Experiment, Methodology. Linhua Gan: Experiment, Resource, Methodology. Holly M. Brown-Borg: Writing-Review&Editing. Wei Feng: Methodology, Writing-Review&Editing, Funding acquisition, Resource, Supervision, Project administration. Yu Chen: Methodology, Writing-Review&Editing, Funding acquisition, Resource, Supervision, Project administration. Robert Chunhua Zhao: Methodology, Writing-Review&Editing, Funding acquisition, Resource, Supervision, Project administration.

Declaration of competing interest

The authors declare that they have no known competing financial

interests or personal relationships that could have appeared to influence the work reported in this paper.

Data availability

Data will be made available on request.

Acknowledgments

Appendix A. Supplementary data

Supplementary data to this article can be found online at https://doi.org/10.1016/j.mtbio.2023.100544.

References

[1] C.D. Wiley, J. Campisi, The metabolic roots of senescence: mechanisms and opportunities for intervention, Nat Metab 3 (10) (2021) 1290–1301, https://doi.org/10.1038/s42255-021-00483-8.

[2] N. Habib, C. McCabe, S. Medina, M. Varshavsky, D. Kitsberg, R. Dvir-Szternfeld, G. Green, D. Dionne, L. Nguyen, J.L. Marshall, F. Chen, F. Zhang, T. Kaplan, A. Regev, M. Schwartz, Disease-associated astrocytes in Alzheimer's disease and aging, Nat. Neurosci. 23 (6) (2020) 701, https://doi.org/10.1038/s41593-020-0624-8.

[3] E.S. Huang, N. Laiteerapong, J.Y. Liu, P.M. John, H.H. Moffet, A.J. Karter, Rates of complications and mortality in older patients with diabetes mellitus the diabetes and aging study, JAMA Intern. Med. 174 (2) (2014) 251–258, https://doi.org/10.1001/jamainternmed.2013.12956.

[4] B.G. Childs, M. Gluscevic, D.J. Baker, R.M. Laberge, D. Marquess, J. Dananberg, J.M. van Deursen, Senescent cells: an emerging target for diseases of ageing, Nat. Rev. Drug Discov. 16 (10) (2017) 718–735, https://doi.org/10.1038/nrd.2017.116.

[5] D.I. Podolskiy, A.V. Lobanov, G.V. Kryukov, V.N. Gladyshev, Analysis of cancer genomes reveals basic features of human aging and its role in cancer development, Nat. Commun. 7 (2016), https://doi.org/10.1038/ncomms12157.

[6] C. Lopez-Otin, M.A. Blasco, L. Partridge, M. Serrano, G. Kroemer, The hallmarks of aging, Cell 153 (6) (2013) 1194–1217, https://doi.org/10.1016/j.cell.2013.05.039.

[7] R. Kumari, P. Jat, Mechanisms of cellular senescence: cell cycle arrest and senescence associated secretory phenotype, Front. Cell Dev. Biol. 9 (2021), https://doi.org/10.3389/Fcell.2021.645593.

[8] J.D. Zheng, Q. Zeng, R.J. Zhang, D. Xing, T. Zhang, Dynamic-reversible photoacoustic probe for continuous ratiometric sensing and imaging of redox status in vivo, J. Am. Chem. Soc. 141 (49) (2019) 19226–19230, https://doi.org/10.1021/jacs.9b10353.

[9] L.X. Liang, L.W. Wen, Y.Q. Weng, J.X. Song, H.H. Li, Y. Zhang, X. He, W. Zhao, M.X. Zhan, Y. Li, L.G. Lu, Y.J. Xin, C.X. Lu, Homologous-targeted and tumor microenvironment-activated hydroxyl radical nanogenerator for enhanced chemoimmunotherapy of non-small cell lung cancer, Chem. Eng. J. 425 (2021), https://doi.org/10.1016/j.cej.2021.131451.

[10] A. Karakoti, S. Singh, J.M. Dowding, S. Seal, W.T. Self, Redox-active radical scavenging nanomaterials, Chem. Soc. Rev. 39 (11) (2010) 4422–4432, https://doi.org/10.1039/b919677n.

[11] H.J. Forman, H.Q. Zhang, Targeting oxidative stress in disease: promise and limitations of antioxidant therapy (Jun, 10.1038/s41573-021-00233-1, 2021), Nat. Rev. Drug Discov. 20 (8) (2021) 652, https://doi.org/10.1038/s41573-021-00267-5, 652.

[12] M.Y. Kang, H.B. Kim, C. Piao, K.H. Lee, J.W. Hyun, I.Y. Chang, H.J. You, The critical role of catalase in prooxidant and antioxidant function of p53, Cell Death Differ. 20 (1) (2013) 117–129, https://doi.org/10.1038/cdd.2012.102.

[13] C.K. Tsang, Y. Liu, J. Thomas, Y.J. Zhang, X.F.S. Zheng, Superoxide dismutase 1 acts as a nuclear transcription factor to regulate oxidative stress resistance, Nat. Commun. 5 (2014), https://doi.org/10.1038/ncomms4446.

[14] M.M. Pinney, D.A. Mokhtari, E. Akiva, F. Yabukarski, D.M. Sanchez, R.B. Liang, T. Doukov, T.J. Martinez, P.C. Babbitt, D. Herschlag, Parallel molecular mechanisms for enzyme temperature adaptation, Science 371 (6533) (2021) 1010–+, https://doi.org/10.1126/science.aay2784.

[15] H. Wei, E.K. Wang, Nanomaterials with enzyme-like characteristics (nanozymes): next-generation artificial enzymes, Chem. Soc. Rev. 42 (14) (2013) 6060–6093, https://doi.org/10.1039/c3cs35486e.

[16] S.A. Muhammad, L.S. Bilbis, Y. Saidu, Y. Adamu, Effect of antioxidant mineral elements supplementation in the treatment of hypertension in albino rats, Oxid. Med. Cell. Longev. (2012), https://doi.org/10.1155/2012/134723, 2012.

[17] H. Huang, Y. Chen, Materdicine, And medmaterial, J. Inorg. Mater. 37 (11) (2022) 1151–1169, https://doi.org/10.15541/jim20220194.

[18] X.Y. Lu, S.S. Gao, H. Lin, L.D. Yu, Y.H. Han, P.A. Zhu, W.C. Bao, H.L. Yao, Y. Chen, J.L. Shi, Bioinspired copper single-atom catalysts for tumor parallel catalytic therapy, Adv. Mater. 32 (36) (2020), https://doi.org/10.1002/adma.202002246.

[19] Q.J. Weng, H. Sun, C.Y. Fang, F. Xia, H.W. Liao, J.Y. Lee, J.C. Wang, A. Xie, J.F. Ren, X. Guo, F.Y. Li, B. Yang, D.S. Ling, Catalytic activity tunable ceria nanoparticles prevent chemotherapy-induced acute kidney injury without interference with chemotherapeutics, Nat. Commun. 12 (1) (2021), https://doi.org/10.1038/s41467-021-21714-2.

[20] A. Watanabe, M. Kajita, J. Kim, A. Kanayama, K. Takahashi, T. Mashino, Y. Miyamoto, In vitro free radical scavenging activity of platinum nanoparticles, Nanotechnology 20 (45) (2009), https://doi.org/10.1088/0957-4484/20/45/455105.

[21] A.A. Vernekar, D. Sinha, S. Srivastava, P.U. Paramasivam, P. D'Silva, G. Mugesh, An antioxidant nanozyme that uncovers the cytoprotective potential of vanadia nanowires, Nat. Commun. 5 (2014), https://doi.org/10.1038/ncomms6301.

[22] W. Feng, X.G. Han, X. Hu, M.Q. Chang, L. Ding, H.J. Xiang, Y. Chen, Y.H. Li, 2D vanadium carbide MXenzyme to alleviate ROS-mediated inflammatory and neurodegenerative diseases, Nat. Commun. 12 (1) (2021), https://doi.org/10.1038/s41467-021-22278-x.

[23] H. Katsumi, K. Fukui, K. Sato, S. Maruyama, S. Yamashita, E. Mizumoto, K. Kusamori, M. Oyama, M. Sano, T. Sakane, A. Yamamoto, Pharmacokinetics and preventive effects of platinum nanoparticles as reactive oxygen species scavengers on hepatic ischemia/reperfusion injury in mice, Metallomics 6 (5) (2014) 1050–1056, https://doi.org/10.1039/c4mt00018h.

[24] H.J. Kwon, M.Y. Cha, D. Kim, D.K. Kim, M. Soh, K. Shin, T. Hyeon, I. Mook-Jung, Mitochondria-targeting ceria nanoparticles as antioxidants for Alzheimer's disease, ACS Nano 10 (2) (2016) 2860–2870, https://doi.org/10.1021/acsnano.5b08045.

[25] H.J. Kwon, D. Kim, K. Seo, Y.G. Kim, S.I. Han, T. Kang, M. Soh, T. Hyeon, Ceria nanoparticle systems for selective scavenging of mitochondrial, intracellular, and extracellular reactive oxygen species in Parkinson's disease, Angew. Chem., Int. Ed. 57 (30) (2018) 9408–9412, https://doi.org/10.1002/anie.201805052.

[26] D.L. Ni, D.W. Jiang, C.J. Kutyreff, J.H. Lai, Y.J. Yan, T.E. Barnhart, B. Yu, H.J. Im, L. Kang, S.Y. Cho, Z.F. Liu, P. Huang, J.W. Engle, W.B. Cai, Molybdenum-based nanoclusters act as antioxidants and ameliorate acute kidney injury in mice, Nat. Commun. 9 (2018), https://doi.org/10.1038/s41467-018-07890-8.

[27] R.Z. Tian, J.Y. Xu, Q.A. Luo, C.X. Hou, J.Q. Liu, Rational design and biological application of antioxidant nanozymes, Front. Chem. 8 (2021), https://doi.org/10.3389/fchem.2020.00831.

[28] K.L. Fan, J.Q. Xi, L. Fan, P.X. Wang, C.H. Zhu, Y. Tang, X.D. Xu, M.M. Liang, B. Jiang, X.Y. Yan, L.Z. Gao, In vivo guiding nitrogen-doped carbon nanozyme for tumor catalytic therapy, Nat. Commun. 9 (2018), https://doi.org/10.1038/s41467-018-03903-8.

[29] W.W. Zeng, X.X. Wu, T. Chen, S.J. Sun, Z.F. Shi, J. Liu, X.Y. Ji, X.W. Zeng, J. Guan, L. Mei, M.Y. Wu, Renal-clearable ultrasmall polypyrrole nanoparticles with size-regulated property for second near-infrared light-mediated photothermal therapy, Adv. Funct. Mater. 31 (15) (2021), https://doi.org/10.1002/adfm.202008362.

[30] X.J. Zhang, S.J. Lin, S.W. Liu, X.L. Tan, Y. Dai, F. Xia, Advances in organometallic/organic nanozymes and their applications, Coord. Chem. Rev. 429 (2021), https://doi.org/10.1016/j.ccr.2020.213652.

[31] M. Kohri, Artificial melanin particles: new building blocks for biomimetic structural coloration, Polym. J. 51 (11) (2019) 1127–1135, https://doi.org/10.1038/s41428-019-0231-2.

[32] H. Liu, X. Qu, H.Q. Tan, J.L. Song, M. Lei, E. Kim, G.F. Payne, C.S. Liu, Role of polydopamine's redox-activity on its pro-oxidant, radical-scavenging, and antimicrobial activities, Acta Biomater. 88 (2019) 181–196, https://doi.org/10.1016/j.actbio.2019.02.032.

[33] X.F. Bao, J.H. Zhao, J. Sun, M. Hu, X.R. Yang, Polydopamine nanoparticles as efficient scavengers for reactive oxygen species in periodontal disease, ACS Nano 12 (9) (2018) 8882–8892, https://doi.org/10.1021/acsnano.8b04022.

[34] H. Zhao, Z.D. Zeng, L. Liu, J.W. Chen, H.T. Zhou, L.L. Huang, J. Huang, H. Xu, Y.Y. Xu, Z.R. Chen, Y. Wu, W.L. Guo, J.H. Wang, J. Wang, Z. Liu, Polydopamine nanoparticles for the treatment of acute inflammation-induced injury, Nanoscale 10 (15) (2018) 6981–6991, https://doi.org/10.1039/c8nr00838h.

[35] T.F. Liu, B.W. Xiao, F. Xiang, J.L. Tan, Z. Chen, X.R. Zhang, C.Z. Wu, Z.W. Mao, G.X. Luo, X.Y. Chen, J. Deng, Ultrasmall copper-based nanoparticles for reactive oxygen species scavenging and alleviation of inflammation related diseases, Nat. Commun. 11 (1) (2020), https://doi.org/10.1038/S41467-020-16544-7.

[36] B.J. Du, X.Y. Jiang, A. Das, Q.H. Zhou, M.X. Yu, R.C. Jin, J. Zheng, Glomerular barrier behaves as an atomically precise bandpass filter in a sub-nanometre regime, Nat. Nanotechnol. 12 (11) (2017) 1096, https://doi.org/10.1038/Nnano.2017.170.+.

[37] Q.R. Zhang, Q.G. Yang, P. Phanlavong, Y.X. Li, Z.K. Wang, T.F. Jiao, Q.M. Peng, Highly efficient lead(II) sequestration using size-controllable polydopamine microspheres with superior application capability and rapid capture, Acs Sustain Chem Eng 5 (5) (2017) 4161–4170, https://doi.org/10.1021/acssuschemeng.7b00129.

[38] D.Y. Zhang, M.R. Younis, H.K. Liu, S. Lei, Y.L. Wan, J.L. Qu, J. Lin, P. Huang, Multi-enzyme mimetic ultrasmall iridium nanozymes as reactive oxygen/nitrogen species

scavengers for acute kidney injury management, Biomaterials 271 (2021), https://doi.org/10.1016/j.biomaterials.2021.120706.

[39] H.C. Huang, C.J. Lin, W.J. Liu, R.R. Jiang, Z.F. Jiang, Dual effects of curcumin on neuronal oxidative stress in the presence of Cu(II), Food Chem. Toxicol. 49 (7) (2011) 1578–1583, https://doi.org/10.1016/j.fct.2011.04.004.

[40] S.C. Chiang, M. Meagher, N. Kassouf, M. Hafezparast, P.J. McKinnon, R. Haywood, S.F. El-Khamisy, Mitochondrial protein-linked DNA breaks perturb mitochondrial gene transcription and trigger free radical-induced DNA damage, Sci. Adv. 3 (4) (2017), https://doi.org/10.1126/sciadv.1602506.

[41] P. Zhu, Y. Chen, J.L. Shi, Piezocatalytic tumor therapy by ultrasound-triggered and BaTiO3-mediated piezoelectricity, Adv. Mater. 32 (29) (2020), https://doi.org/10.1002/adma.202001976.

[42] T. Irrazabal, B.K. Thakur, M.S. Kang, Y. Malaise, C. Streutker, E.O.Y. Wong, J. Copeland, R. Gryfe, D.S. Guttman, W.W. Navarre, A. Martin, Limiting oxidative DNA damage reduces microbe-induced colitis-associated colorectal cancer, Nat. Commun. 11 (1) (2020), https://doi.org/10.1038/s41467-020-15549-6.

[43] J.R. Radke, I. Figueroa, J.M. Routes, J.L. Cook, PIDD-dependent activation of caspase-2-mediated mitochondrial injury in E1A-induced cellular sensitivity to macrophage nitric oxide-induced apoptosis, Cell Death Dis. 4 (2018), https://doi.org/10.1038/s41420-018-0100-3.

[44] S. Sonoda, Y.F. Mei, I. Atsuta, A. Danjo, H. Yamaza, S. Hama, K. Nishida, R.H. Tang, Y. Kyumoto-Nakamura, N. Uehara, T. Kukita, F. Nishimura, T. Yamaza, Exogenous nitric oxide stimulates the odontogenic differentiation of rat dental pulp stem cells, Sci Rep-Uk 8 (2018), https://doi.org/10.1038/s41598-018-21183-6.

[45] A. Robaszkiewicz, G. Bartosz, Estimation of antioxidant capacity against pathophysiologically relevant oxidants using Pyrogallol Red, Biochem Bioph Res Co 390 (3) (2009) 659–661, https://doi.org/10.1016/j.bbrc.2009.10.023.

[46] C.T. Chen, F.J. Martin-Martinez, G.S. Jung, M.J. Buehler, Polydopamine and eumelanin molecular structures investigated with ab initio calculations, Chem. Sci. 8 (2) (2017) 1631–1641, https://doi.org/10.1039/c6sc04692d.

[47] L. Panzella, G. Gentile, G. D'Errico, N.F. Della Vecchia, M.E. Errico, A. Napolitano, C. Carfagna, M. d'Ischia, Atypical structural and pi-electron features of a melanin polymer that lead to superior free-radical-scavenging properties, Angew. Chem., Int. Ed. 52 (48) (2013) 12684–12687, https://doi.org/10.1002/anie.201305747.

[48] A.A.R. Watt, J.P. Bothma, P. Meredith, The supramolecular structure of melanin, Soft Matter 5 (19) (2009) 3754–3760, https://doi.org/10.1039/b902507c.

[49] E. Kim, M. Kang, T. Tschirhart, M. Malo, E. Dadachova, G. Cao, J.J. Yin, W.E. Bentley, Z. Wang, G.F. Payne, Spectroelectrochemical reverse engineering demonstrates that melanin's redox and radical scavenging activities are linked, Biomacromolecules 18 (12) (2017) 4084–4098, https://doi.org/10.1021/acs.biomac.7b01166.

[50] J.H. Zhang, Y. Fu, P. Yang, X.H. Liu, Y.W. Li, Z.P. Gu, ROS scavenging biopolymers for anti-inflammatory diseases: classification and formulation, Adv. Mater. Interfac. 7 (16) (2020), https://doi.org/10.1002/admi.202000632.

[51] M.P. Baar, R.M.C. Brandt, D.A. Putavet, J.D.D. Klein, K.W.J. Derks, B.R.M. Bourgeois, S. Stryeck, Y. Rijksen, H. van Willigenburg, D.A. Feijtel, I. van der Pluijm, J. Essers, W.A. van Cappellen, W.F. van Ijcken, A.B. Houtsmuller, J. Pothof, R.W.F. de Bruin, T. Madl, J.H.J. Hoeijmakers, J. Campisi, P.L.J. de Keizer, Targeted apoptosis of senescent cells restores tissue homeostasis in response to chemotoxicity and aging, Cell 169 (1) (2017) 132–+, https://doi.org/10.1016/j.cell.2017.02.031.

[52] W. Rao, H. Wang, J.F. Han, S.T. Zhao, J. Dumbleton, P. Agarwal, W.J. Zhang, G. Zhang, J.H. Yu, D.L. Zynger, X.B. Lu, X.M. He, Chitosan-decorated doxorubicin-encapsulated nanoparticle targets and eliminates tumor reinitiating cancer stem-like cells, ACS Nano 9 (6) (2015) 5725–5740, https://doi.org/10.1021/nn506928p.

[53] H. Yoo, H.S. Kim, Cacao powder supplementation attenuates oxidative stress, cholinergic impairment, and apoptosis in d-galactose-induced aging rat brain, Sci Rep-Uk 11 (1) (2021), https://doi.org/10.1038/s41598-021-96800-y.

[54] B.Y. Lee, J.A. Han, J.S. Im, A. Morrone, K. Johung, E.C. Goodwin, W.J. Kleijer, D. DiMaio, E.S. Hwang, Senescence-associated beta-galactosidase is lysosomal beta-galactosidase, Aging Cell 5 (2) (2006) 187–195, https://doi.org/10.1111/j.1474-9726.2006.00199.x.

[55] J.Y. Liu, G.P. Souroullas, B.O. Diekman, J. Krishnamurthy, B.M. Hall, J.A. Sorrentino, J.S. Parker, G.A. Sessions, A.V. Gudkov, N.E. Sharpless, Cells exhibiting strong p16 (INK4a) promoter activation in vivo display features of senescence, Proc. Natl. Acad. Sci. U. S. A. 116 (7) (2019) 2603–2611, https://doi.org/10.1073/pnas.1818313116.

[56] A. Helman, A. Klochendler, N. Azazmeh, Y. Gabai, E. Horwitz, S. Anzi, A. Swisa, R. Condiotti, R.Z. Granit, Y. Nevo, Y. Fixler, D. Shreibman, A. Zamir, S. Tornovsky-Babeay, C. Dai, B. Glaser, A.C. Powers, A.M. Shapiro, M.A. Magnuson, Y. Dor, I. Ben-Porath, p16(Ink4a)-induced senescence of pancreatic beta cells enhances insulin secretion, Nat. Med. 22 (4) (2016) 412–420, https://doi.org/10.1038/nm.4054.

[57] D.H. Ho, W. Seol, I. Son, Upregulation of the p53-p21 pathway by G2019S LRRK2 contributes to the cellular senescence and accumulation of alpha-synuclein, Cell Cycle 18 (4) (2019) 467–475, https://doi.org/10.1080/15384101.2019.1577666.

[58] J. Chen, K.H. Chen, F. Xiao, H.Z. Dai, J. Yang, L.M. Wang, X.Y. Wang, J.G. Zhang, Y.N. He, Decoy receptor 2 mediation of the senescent phenotype of tubular cells by interacting with peroxiredoxin 1 presents a novel mechanism of renal fibrosis in

diabetic nephropathy, Kidney Int. 98 (3) (2020) 645–662, https://doi.org/10.1016/j.kint.2020.03.026.

[59] B. Bourgeois, T. Madl, Regulation of cellular senescence via the FOXO4-p53 axis, FEBS Lett. 592 (12) (2018) 2083–2097, https://doi.org/10.1002/1873-3468.13057.

[60] E. Lukasova, A. Kovarik, S. Kozubek, Consequences of lamin B1 and lamin B receptor downregulation in senescence, Cells-Basel 7 (2) (2018), https://doi.org/10.3390/Cells7020011.

[61] A. Freund, R.M. Laberge, M. Demaria, J. Campisi, Lamin B1 loss is a senescence-associated biomarker, Mol. Biol. Cell 23 (11) (2012) 2066–2075, https://doi.org/10.1091/mbc.E11-10-0884.

[62] S. Dassati, A. Waldner, R. Schweigreiter, Apolipoprotein D takes center stage in the stress response of the aging and degenerative brain, Neurobiol. Aging 35 (7) (2014) 1632–1642, https://doi.org/10.1016/j.neurobiolaging.2014.01.148.

[63] E. Zoico, S. Rubele, A. De Caro, N. Nori, G. Mazzali, F. Fantin, A. Rossi, M. Zamboni, Brown and beige adipose tissue and aging, Front. Endocrinol. 10 (2019), https://doi.org/10.3389/Fendo.2019.00368.

[64] P. Gu, X.Y. Hui, Q.T. Zheng, Y. Gao, L.G. Jin, W.M. Jiang, C.S. Zhou, T.X. Liu, Y. Huang, Q. Liu, T. Nie, Y.F. Wang, Y. Wang, J.G. Zhao, A.M. Xu, Mitochondrial uncoupling protein 1 antagonizes atherosclerosis by blocking NLRP3 inflammasome-dependent interleukin-1 beta production, Sci. Adv. 7 (50) (2021), https://doi.org/10.1126/sciadv.abl4024.

[65] S. Cadenas, Mitochondrial uncoupling, ROS generation and cardioprotection, Bba-Bioenergetics 1859 (9) (2018) 940–950, https://doi.org/10.1016/j.bbabio.2018.05.019.

[66] L.L. Sun, J.Y. Chiang, J.Y. Choi, Z.M. Xiong, X.J. Mao, F.S. Collins, R.J. Hodes, K. Cao, Transient induction of telomerase expression mediates senescence and reduces tumorigenesis in primary fibroblasts, P Natl Acad Sci USA 116 (38) (2019) 18983–18993, https://doi.org/10.1073/pnas.1907199116.

[67] M.L. Calio, D.S. Marinho, G.M. Ko, M. Porcionatto, Antioxidant effect of leptin on neurogenic niches in a model of Alzheimer's disease, Free Radical Biol. Med. 100 (2016) S159, https://doi.org/10.1016/j.freeradbiomed.2016.10.416. S159.

[68] C. Molinari, V. Morsanuto, S. Ruga, F. Notte, M. Farghali, R. Galla, F. Uberti, The role of BDNF on aging-modulation markers, Brain Sci. 10 (5) (2020), https://doi.org/10.3390/Brainsci10050285.

[69] S.Y. Wu, B.S. Pan, S.F. Tsai, Y.T. Chiang, B.M. Huang, F.E. Mo, Y.M. Kuo, BDNF reverses aging-related microglial activation, J. Neuroinflammation 17 (1) (2020), https://doi.org/10.1186/s12974-020-01887-1.

[70] A. Salminen, A. Kauppinen, K. Kaarniranta, Emerging role of NF-kappa B signaling in the induction of senescence-associated secretory phenotype (SASP), Cell. Signal. 24 (4) (2012) 835–845, https://doi.org/10.1016/j.cellsig.2011.12.006.

[71] X.L. Wang, X.X. Sun, M.Y. Niu, X.N. Zhang, J. Wang, C. Zhou, A.M. Xie, RAGE silencing ameliorates neuroinflammation by inhibition of p38-NF-kappa B signaling pathway in mouse model of Parkinson's disease, Front Neurosci-Switz 14 (2020), https://doi.org/10.3389/Fnins.2020.00353.

[72] E. Aoyama, E. Kubota, H.M. Khattab, T. Nishida, M. Takigawa, CCN2 enhances RANKL-induced osteoclast differentiation via direct binding to RANK and OPG, Bone 73 (2015) 242–248, https://doi.org/10.1016/j.bone.2014.12.058.

[73] T. Hirano, IL-6 in inflammation, autoimmunity and cancer, Int. Immunol. 33 (3) (2021) 127–148, https://doi.org/10.1093/intimm/dxaa078.

[74] L. Zhan, H.Y. Cao, G. Wang, Y.H. Lyu, X.C. Sun, J.Z. An, Z.B. Wu, Q.C. Huang, B.R. Liu, J.L. Xing, Drp1-mediated mitochondrial fission promotes cell proliferation through crosstalk of p53 and NF-kappa B pathways in hepatocellular carcinoma, Oncotarget 7 (40) (2016) 65001–65011, https://doi.org/10.18632/oncotarget.11339.

[75] E.S. Jun, Y.J. Kim, H.H. Kim, S.Y. Park, Gold nanoparticles using ecklonia stolonifera protect human dermal fibroblasts from UVA-induced senescence through inhibiting MMP-1 and MMP-3, Mar. Drugs 18 (9) (2020), https://doi.org/10.3390/Md18090433.

[76] R. Minami, K. Muta, T. Umemura, S. Motomura, Y. Abe, J. Nishimura, H. Nawata, p16(INK4a) induces differentiation and apoptosis in erythroid lineage cells, Exp. Hematol. 31 (5) (2003) 355–362, https://doi.org/10.1016/S0301-472x(03)00040-7.

[77] X.J. Wang, K.M. Kong, W.L. Qi, W.L. Ye, P.S. Song, Interleukin-1 beta induction of neuron apoptosis depends on p38 mitogen-activated protein kinase activity after spinal cord injury, Acta Pharmacol. Sin. 26 (8) (2005) 934–942, https://doi.org/10.1111/j.1745-7254.2005.00152.x.

[78] T. Takeda, M. Hosokawa, K. Higuchi, Senescence-accelerated mouse (SAM): a novel murine model of senescence, Exp. Gerontol. 32 (1–2) (1997) 105–109, https://doi.org/10.1016/S0531-5565(96)00036-8.

[79] R. Varga, M. Eriksson, M.R. Erdos, M. Olive, I. Harten, F. Koldgie, B.C. Capell, J. Cheng, D. Faddah, S. Perkins, H. Avallone, H. San, X. Qu, S. Ganesh, L.B. Gordon, R. Virmani, T.N. Wight, E.G. Nabel, F.S. Collins, Progressive vascular smooth muscle cell defects in a mouse model of Hutchinson-Gilford progeria syndrome, P Natl Acad Sci USA 103 (9) (2006) 3250–3255, https://doi.org/10.1073/pnas.0600012103.

[80] A. Bilkei-Gorzo, Genetic mouse models of brain ageing and Alzheimer's disease, Pharmacol. Therapeut. 142 (2) (2014) 244–257, https://doi.org/10.1016/j.pharmthera.2013.12.009.